Monthly Notices of the ROYAL ASTRONOMICAL SOCIETY

MNRAS **527,** 6211–6226 (2024) https://doi.org/10.1093/mnras/stad3632
Advance Access publication 2023 November 24

A study of chemical abundances, rotational velocities, and orbital elements in single-lined spectroscopic binary stars in open clusters

A. A. Ramos,[1] N. Holanda ,[1]★ N. A. Drake ,[1,2] M. J. Rain ,[3] F. F. S. Maia ,[4] S. Daflon [1] and C. B. Pereira[1]

[1]*Observatório Nacional, Rua General José Cristino 77, CEP 20921-400, São Cristóvão, Rio de Janeiro, RJ, Brazil*
[2]*Laboratory of Observational Astrophysics, Saint Petersburg State University, Universitetski pr. 28, 198504, Saint Petersburg, Russia*
[3]*European Southern Observatory, Alonso de Córdova 3107, Vitacura, Región Metropolitana, Chile*
[4]*Instituto de Física, Universidade Federal do Rio de Janeiro, 21941-972, Rio de Janeiro, RJ, Brazil*

Accepted 2023 November 21. Received 2023 November 20; in original form 2023 August 26

ABSTRACT

Binary interactions play a significant role in stellar evolution. In this study, we present a comprehensive analysis of 17 single-lined spectroscopic binary stars and identify two more as 'yellow stragglers', in the context of 15 young open clusters with ages younger than 1.0 Gyr. High-resolution spectroscopy ($R \approx 48000$) was employed to determine atmospheric parameters and chemical abundances of various elements including Li, C (C_2), N (^{12}CN), O, Na, Mg, Al, Ca, Si, Ti, Ni, Cr, Y, Zr, La, Ce, Nd, and Eu, and compared them with the abundances of stars reported in the literature. The projected rotational velocities (v sin i) of 17 stars were determined via the spectral synthesis method. For two stars, we analyse the phenomenon of yellow stragglers based on their spectra and colour–magnitude diagram. Our v sin i results exhibit excellent agreement with previous studies in the literature for four stars previously analysed. Furthermore, we found a similar set of chemical abundances between thin disc stars and the studied spectroscopic binaries, except for s-process elements, such as La, Ce, and Nd. Also, we confirm that yellow straggler stars are members of binary systems, specifically giant G/K-type stars paired with dwarf A-type stars. Finally, we investigated the relationships between chemical abundances, orbital parameters (obtained from the literature), and v sin i, which can provide insights into the observed anomalies in ^{7}Li abundance in two stars such as NGC 6694-14 and NGC 6709-303. Our findings suggest that the anomalous rotation and lithium enrichment observed in these stars are likely results of interactions within binary companions.

Key words: stars: abundances – (stars:) binaries: spectroscopic – stars: fundamental parameters.

1 INTRODUCTION

The majority of stars in the Galaxy are known to be formed within compact clusters, accounting for approximately 70–90 per cent of all star formation events (Lada & Lada 2003). Among these clusters, open clusters hold great significance as they provide valuable insights into Galactic chemical evolution and stellar evolution models. Open clusters are abundant, relatively young, and widely distributed throughout the Galactic disc, making them ideal targets for studying stellar populations and their evolution (e.g. Friel 1995; Hekker & Meléndez 2007; Magrini et al. 2009; Reddy & Lambert 2019). Furthermore, the presence of binary star systems within open clusters is of particular interest, as gravitational interactions among binary members can significantly influence the structure and evolutionary path of a cluster. Studying binary populations in open clusters offers crucial information about fundamental stellar properties and contributes to our understanding of stellar evolution (see Duchêne & Kraus 2013; Albrow & Ulusele 2022).

Various authors have employed techniques like radial velocities and photometry, applied to colour–magnitude diagrams (CMDs) or time series, to identify binary stars in open clusters. Mermilliod & Mayor (1989) observed a percentage of spectroscopic binaries (SBs) ranging from 25 per cent to 33 per cent in five open clusters with ages similar to the Hyades cluster (NGC 2447, NGC 2539, NGC 6633, and NGC 6940). They also identified systems in the Hertzsprung Gap, consisting of a G/K giant and an A dwarf star, which might be associated with yellow stragglers (YSs). YSs are stars that appear anomalously young and hot for their position in the CMD. One possible channel in stellar evolution is the transformation of blue stragglers (BSs), characterized by their higher luminosity compared to stars in the turn-off cluster region, into YSs. The underlying mechanisms driving their formation may involve processes such as mass transfer in close binary systems, stellar collisions, or mergers (Stryker 1993; Boffin et al. 2015; Rain et al. 2020; Rain, Ahumada & Carraro 2021). Other surveys in this context have suggested frequencies of SBs in open clusters ranging from 13 per cent to 20 per cent (Duchêne & Kraus 2013, and references therein). Sollima et al. (2010), using photometric observations, determined the fraction of binary systems in a sample of five open clusters. They found a minimum binary fraction larger than 11 per cent within the core radius and estimated global fractions of binary systems between 35 per cent and 70 per cent. Recently, Jadhav et al. (2021) conducted an analysis to estimate the high-mass ratio (HMR) binary fraction,

★ E-mail: nacizoholanda@on.br

Table 1. General information about the sample. References: Mermilliod et al. (2008)[a] and Cutri et al. (2013)[b]. Radial velocities (RVs; seventh column) and projected rotational velocities (v sin i; eighth column) are determined in this study.

Star	V[a] mag	B−V[a] mag	K[b] mag	V−K mag	⟨RVs⟩[a] km s^{-1}	RVs km s^{-1}	v sin i km s^{-1}	Date Obs. yy mm dd	Exp. s	Remark[a]
IC 2488-97	9.409	1.394	6.097	3.312	−02.48 ± 0.52	−04.51 ± 0.68	5.2 ± 0.3	2016 Mar 23	1200	SB
IC 2714-34	10.625	1.571	6.629	3.996	−17.76 ± 0.14	−17.80 ± 0.30	2.1 ± 0.1	2009 Mar 09	1800	SB?
NGC 2215-26	10.525	1.135	7.861	2.664	−03.43 ± 0.12	−08.95 ± 0.68	3.1 ± 0.2	2016 Oct 01	1800	SB1O
NGC 2287-21	6.926	1.516	3.570	3.356	+23.22 ± 0.07	+25.16 ± 0.63	3.3 ± 0.2	2008 Oct 19	420	SB1O
NGC 2287-97	7.755	1.147	5.206	2.549	+22.83 ± 0.10	+22.93 ± 0.15	3.8 ± 0.2	2008 Oct 17	420	SB1O
NGC 2287-102	7.282	0.577	5.040	2.242	+23.40 ± 0.14	+19.10 ± 0.02	–	2016 May 14	420	SB1O
NGC 2287-107	7.769	1.154	5.204	2.565	+23.34 ± 0.05	+20.15 ± 1.20	4.0 ± 0.1	2008 Oct 19	420	SB1O
NGC 2335-4	9.480	1.400	6.157	3.323	+21.82 ± 0.10	+19.77 ± 0.39	7.3 ± 0.2	2016 Mar 12	1200	SB1O
NGC 2423-43	10.480	1.020	8.017	2.463	+18.75 ± 0.16	+19.07 ± 0.18	3.8 ± 0.1	2008 Dec 22	900	SB1O
NGC 2548-1260	9.065	0.525	7.247	1.818	+09.46 ± 0.51	+04.12 ± 0.47	–	2008 Dec 23	420	SB
NGC 2548-1560	8.215	1.140	5.420	2.795	+08.27 ± 0.15	+03.06 ± 0.88	3.4 ± 0.2	2008 Dec 25	300	SB1O
NGC 2925-92	9.393	1.309	6.927	2.466	+12.68 ± 0.07	+06.70 ± 0.31	3.0 ± 0.1	2016 Mar 21	1200	SB1O
NGC 2972-14	9.401	1.762	5.308	4.093	+21.09 ± 0.09	+24.55 ± 0.44	6.9 ± 0.2	2016 Mar 19	900	SB1O
NGC 6067-240	9.990	1.700	6.161	3.829	−40.00 ± 1.94	−42.72 ± 0.20	4.2 ± 0.2	2009 Aug 03	1200	SB
NGC 6664-52	10.330	1.959	5.650	4.680	+21.02 ± 0.70	+23.68 ± 1.84	6.5 ± 0.2	2009 Aug 04	1200	SB
NGC 6664-53	10.750	2.132	5.808	4.942	+16.91 ± 3.64	+14.06 ± 0.52	4.1 ± 0.2	2009 Aug 04	1800	SB
NGC 6664-54	10.810	2.104	5.401	5.409	+19.00 ± 0.13	+40.92 ± 0.38	5.3 ± 0.2	2009 Aug 05	1800	SB1O
NGC 6694-14	10.300	1.490	6.038	4.262	−08.51 ± 0.10	−07.37 ± 0.60	7.5 ± 0.2	2016 Jun 11	1400	SB1O
NGC 6709-303	9.041	1.312	5.880	3.161	−09.53 ± 0.11	+05.78 ± 0.38	7.1 ± 0.1	2016 Jul 15	900	SB1O

both total and spectral-type, in 23 open clusters. Their approach involved studying unresolved binaries in CMDs using data from Gaia DR2. The study found that in open clusters, the HMR binary fraction for stars with masses ranging from early M- to late B-types exhibited a range of 0.12–0.38, with a peak at 0.12–0.20. Additionally, there was a decreasing trend in the total binary fraction from late B- to K-type stars, consistent with Galactic field stars.

In addition to their role in understanding the evolution of open clusters, binary star systems can also provide valuable insights into chemical abundance patterns in the Galaxy. Discussions about chemically peculiar stars in open clusters and field stars (Pereira et al. 2011; Santrich, Pereira & Drake 2013; Van der Swaelmen et al. 2017; Karinkuzhi et al. 2018), Li-rich giants (Delgado Mena et al. 2016; Jorissen et al. 2020; Holanda, Drake & Pereira 2020a, b; Tsantaki et al. 2023), C-rich and C-deficient stars (Bond 2019; Holanda, Drake & Pereira 2023), among others, may find clues in the interaction processes between binary components thanks to episodes such as mass-transfer, material accretion, and tidal effects.

In continuation of prior investigations exploring chemical abundances of evolved stars in young open clusters (da Silveira, Pereira & Drake 2018; Holanda, Pereira & Drake 2019; Martinez et al. 2020; Holanda et al. 2021, 2022), the primary focus of this research lies on conducting a comprehensive study of a sample of 17 single-lined spectroscopic binaries stars identified in southern open clusters. Also, the main objectives of this study encompass the characterization of two YS candidate objects, taking into account colours and spectral analysis. Optical high-resolution spectra of spectroscopic binary stars studied in a radial-velocity survey by Mermilliod et al. (2007a), Mermilliod, Mayor & Udry (2008) form the basis of the present study. The paper is organized as follows: in Section 2, we describe the data set and their analysis. In Section 3, we present our results for abundances and compare them with field stars and mixing predictions. Section 3.4 discusses the YS candidates, their formation, and typical characteristics. In Section 3.5, we present the orbital elements for the spectroscopic binary stars in our sample and discuss their impact on the interpretation of the chemical abundance results. Finally, our summary and conclusions are given in Section 4.

2 OBSERVATIONS AND ANALYSIS

For our analysis, we selected a sample from the radial-velocity survey conducted by Mermilliod et al. (2007a) and Mermilliod, Mayor & Udry (2008). The authors presented comprehensive catalogues resulting from a long-term observational project that adopted two CORAVEL spectrovelocimeters to study 1309 giant stars in open clusters. This project involved conducting membership analysis and calculating average velocities for both stars and open clusters. The authors derived weighted mean radial velocities from a data set comprising 10 517 individual observations, including the systemic radial velocities obtained for binary systems. Our analysis, part of a series of papers (Santrich, Pereira & Drake 2013; Sales Silva et al. 2014; da Silveira, Pereira & Drake 2018; Peña Suárez et al. 2018; Holanda, Pereira & Drake 2019; Martinez et al. 2020; Holanda et al. 2021), focuses specifically on studying a sample of SB within the context of this survey (the sample is listed in Table 1). The 19 stars analysed in this work were selected based on table 5 of Mermilliod, Mayor & Udry (2008). Of these, 13 stars have orbital periods and eccentricities published by Mermilliod et al. (2007a), which are classified as SB1O systems. The other stars included, were at least classified as a spectroscopic binary without orbital parameters determined (SB) and one was classified as a suspected binary (SB?). These parameters are taken into account to discuss the possible effects of binarity on a set of chemical abundances typically used as tracers for identifying extra mixing or accretion material (see Section 3.5).

The 19 spectra used in our study were acquired using the fibre-fed extended range optical spectrograph (FEROS; Kaufer et al. 1999), which is installed on the European Southern Observatory's (ESO) 2.2 m telescope at the La Silla observatory in Chile. FEROS covers a wide spectral range from 3700 to 9200 Å, providing broad coverage of the optical wavelength region. It operates at a high resolving power of approximately R ≈ 48000, allowing for detailed spectral analysis and identification of fine spectral features. To assess the quality of the spectra, we evaluated the signal-to-noise ratio (SNR) by measuring the fluctuation of the rms flux in the continuum; the

Table 2. Stellar atmospheric parameters obtained from spectroscopy and photometry, and comparison with literature results. References: AS17, Alonso-Santiago et al. (2017), AS20, Alonso-Santiago et al. (2020), G89, Gilroy (1989), S12, Santos et al. (2012), and VS17, Van der Swaelmen et al. (2017).

Star	$T_{\rm eff}^{(V-K)}$ K	log $g^{\rm phot}$	$T_{\rm eff}^{\rm spec}$ K	log $g^{\rm spec}$	[Fe I/H]	#	[Fe II/H]	#	$\xi_{\rm t}$ km s^{-1}	Ref.
IC 2488-97	4633 ± 39	1.78	4550 ± 80	1.60 ± 0.20	$+0.15 \pm 0.09$	37	$+0.13 \pm 0.12$	8	1.45 ± 0.10	This work
IC 2714-34	4321 ± 37	1.78	4300 ± 50	1.60 ± 0.20	-0.31 ± 0.08	46	-0.29 ± 0.14	13	1.42 ± 0.10	This work
NGC 2215-26	5076 ± 43	2.62	5050 ± 60	2.40 ± 0.15	-0.04 ± 0.10	71	-0.04 ± 0.11	17	1.45 ± 0.10	This work
NGC 2287-21	4114 ± 35	1.12	4100 ± 110	0.80 ± 0.30	-0.18 ± 0.14	36	-0.18 ± 0.15	9	1.98 ± 0.10	This work
	–	–	4350 ± 82	1.71 ± 0.66	-0.24 ± 0.24	179	-0.24 ± 0.37	24	2.49 ± 0.08	S12
NGC 2287-97	4704 ± 40	1.87	4600 ± 80	1.70 ± 0.30	-0.10 ± 0.12	61	-0.08 ± 0.10	15	1.62 ± 0.10	This work
	–	–	4764 ± 46	2.15 ± 0.40	-0.09 ± 0.14	181	-0.09 ± 0.12	25	1.98 ± 0.04	S12
NGC 2287-107	4692 ± 40	1.87	4690 ± 20	1.90 ± 0.20	-0.02 ± 0.13	61	-0.05 ± 0.12	15	1.64 ± 0.10	This work
NGC 2335-4	5213 ± 44	1.91	4900 ± 60	1.50 ± 0.10	-0.07 ± 0.09	45	-0.04 ± 0.05	06	2.25 ± 0.10	This work
	4750	–	–	1.20	-0.08	–	–	–	1.50	VS17
NGC 2423-43	4915 ± 42	2.60	4835 ± 50	2.30 ± 0.20	$+0.00 \pm 0.09$	57	$+0.01 \pm 0.09$	19	1.30 ± 0.10	This work
NGC 2548-1560	4454 ± 38	1.79	4460 ± 70	1.60 ± 0.15	-0.07 ± 0.10	32	-0.04 ± 0.12	09	1.45 ± 0.10	This work
	–	2.20 ± 0.30	4600 ± 150	–	$+0.00 \pm 0.20$	–	–	–	2.00 ± 0.20	G89
NGC 2925-92	4888 ± 42	2.59	4860 ± 80	2.40 ± 0.25	$+0.31 \pm 0.13$	57	$+0.31 \pm 0.12$	14	1.14 ± 0.10	This work
NGC 2972-14	4470 ± 41	0.98	4325 ± 110	0.80 ± 0.30	-0.17 ± 0.15	27	-0.15 ± 0.15	07	2.39 ± 0.2	This work
NGC 6067-240	4445 ± 38	1.52	4200 ± 60	1.40 ± 0.18	$+0.10 \pm 0.09$	45	$+0.11 \pm 0.10$	12	1.49 ± 0.08	This work
	–	–	4051 ± 106	0.99 ± 0.36	$+0.24 \pm 0.24$	–	–	–	1.71*	AS17
NGC 6664-52	4653 ± 40	1.28	4250 ± 135	0.60 ± 0.20	-0.20 ± 0.12	18	-0.18 ± 0.07	07	1.79 ± 0.15	This work
	–	–	4208 ± 60	0.92 ± 0.17	$+0.00 \pm 0.09$	–	–	–	1.80*	AS20
NGC 6664-53	4443 ± 38	1.31	4200 ± 120	1.15 ± 0.15	$+0.00 \pm 0.12$	26	-0.02 ± 0.05	07	1.69 ± 0.10	This work
	–	–	3960 ± 42	0.68 ± 0.13	-0.10 ± 0.07	–	–	–	1.71*	AS20
NGC 6664-54	4139 ± 35	1.09	4030 ± 150	1.20 ± 0.25	$+0.06 \pm 0.14$	22	$+0.08 \pm 0.05$	06	1.79 ± 0.20	This work
	–	–	4492 ± 46	1.47 ± 0.15	$+0.10 \pm 0.07$	–	–	–	1.65*	AS20
NGC 6694-14	4601 ± 39	1.57	4520 ± 140	1.54 ± 0.20	-0.06 ± 0.10	20	-0.07 ± 0.08	06	1.63 ± 0.10	This work
NGC 6709-303	4912 ± 42	1.92	4780 ± 90	1.90 ± 0.20	-0.05 ± 0.12	33	-0.02 ± 0.09	07	1.86 ± 0.10	This work

*Microturlence velocity obtained via calibrations provided by Adibekyan et al. (2012a; AS17) and Dutra-Ferreira et al. (2016; AS20).

SNR values for the spectra in our sample ranged from 100 to 150 at 6000 Å, indicating a favourable level of data quality for our analysis. NGC 2335-4 was observed under the programme ID 096.A-9024(A). IC 2488-97, NGC 2925-14, and NGC 2972-14 were observed under the programme ID 096.A-9027(A). NGC 2287-102, NGC 6694-14, and NGC 6709-303 were observed under the programme ID 097.A-9024(A). NGC 2215-26 was observed under the programme ID 097.A-9026(A). The other stars were observed under the agreement between Observatório Nacional (Brazil) and ESO.

To perform our spectroscopic analysis, we used the MOOG code (version 2019; Sneden) as the main tool. This software enables spectral line analysis and spectrum synthesis, assuming local thermodynamic equilibrium (LTE) conditions. Also, we incorporated 1D-LTE plane-parallel model atmospheres by Castelli & Kurucz (2004) and employed an interpolator to ensure more precise and accurate results.

2.1 Atmospheric parameters

The determination of atmospheric parameters, including effective temperature ($T_{\rm eff}$), surface gravity (log g), microturbulent velocity ($\xi_{\rm t}$), and metallicity ([Fe/H]), was carried out using the standard spectroscopic method. We employed a set of absorption lines from neutral and single ionized iron (Fe I and Fe II) taken from the compilation provided by Lambert et al. (1996). The original list contains 165 Fe I and 24 Fe II lines, but we selected the best measurements on a line-by-line procedure using IRAF and the *splot* routine (Tody 1986). The final count of measured lines and the corresponding atmospheric parameter set can be found in Table 2.

To derive the effective temperature, we employed an iterative procedure aimed at minimizing the slope of the regression line fitting the Fe I lines abundance against the lower-level excitation potential (χ) associated with those lines. Simultaneously, the microturbulent velocity was determined by minimizing the slope between the Fe I abundance and the reduced equivalent width (EW/λ) values for the corresponding lines (as illustrated in Fig. 1). The surface gravity was obtained by enforcing ionization equilibrium, ensuring similar abundance values for both Fe I and Fe II species. We estimated the uncertainties in the atmospheric parameters using the same methodology as Holanda, Pereira & Drake (2019). The error in the effective temperature was derived from the uncertainty in the slope of the relation [Fe I/H] versus χ. The error in the microturbulent velocity was estimated from the uncertainty in the slope of [Fe I/H] versus log EW/λ. For surface gravity, we iteratively adjusted the log g value until the difference in the average abundances of [Fe I/H] and [Fe II/H] matched the standard deviation of the mean [Fe I/H].

Additionally, we derived photometric temperature and gravity values, often referred to as 'evolutive gravity', as an alternative means to validate the spectroscopic results. The photometric gravities were calculated using the well-known equation

$$\log g_\star = \log\left(\frac{M_{\rm turn-off}}{\rm M_\odot}\right) + 0.4\,(K - A_{\rm K} + BC_{\rm K}) + 4\,\log T_{\rm eff}^{(V-K)} - 2\,\log r\,({\rm kpc}) - 16.5,$$

where $M_{\rm turn\text{-}off}$ represents the turn-off mass of the cluster, K denotes the 2MASS magnitude, $A_{\rm K}$ represents the extinction in the K band, $BC_{\rm K}$ indicates the bolometric correction in the K band, $T_{\rm eff}^{(V-K)}$ represents the effective temperature derived from the $(V-K)_0$ colour using the polynomial relations from Alonso, Arribas & Martínez-Roger (1999), and r represents the distance in kiloparsecs (kpc). The turn-off mass of each cluster was estimated by considering parameters such as age, metallicity, and distance obtained from Dias et al. (2021), as

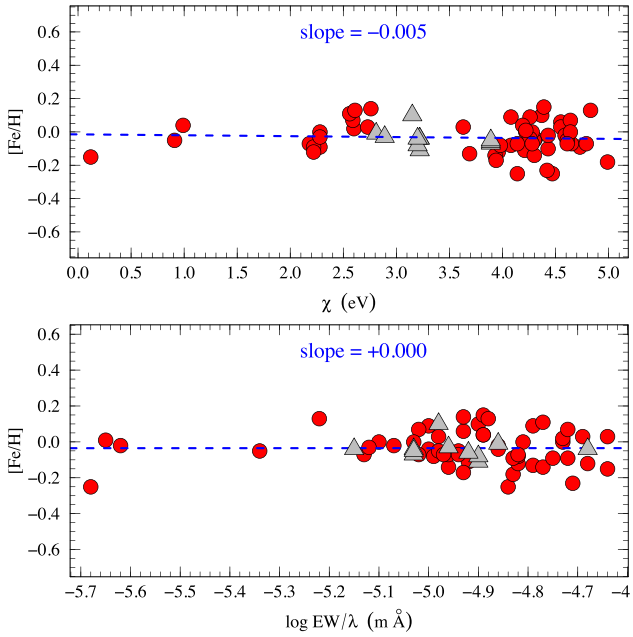

Figure 1. Iron abundances are plotted against excitation potential (χ) and reduced equivalent width (log EW/λ). The blue dashed lines represent the linear regressions, and the individual slopes are indicated in each panel. The regression considers only the Fe I (circles) line abundances, while the Fe II abundances (triangles) are presented for comparison purposes.

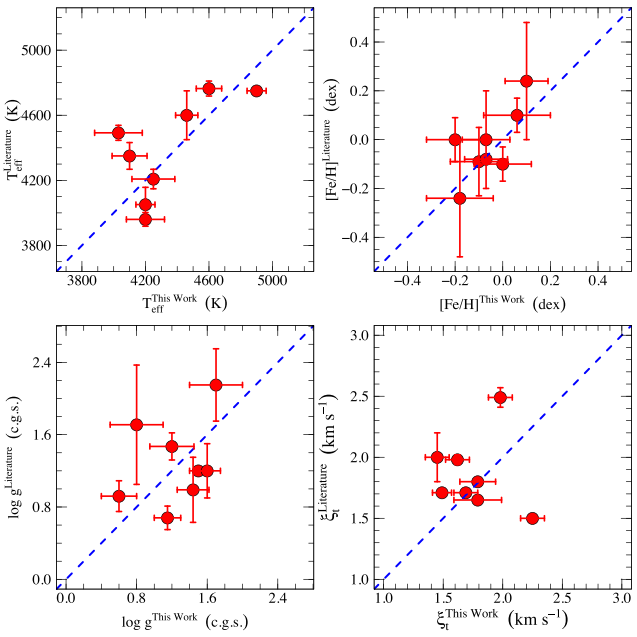

Figure 2. Comparison of atmospheric parameters derived from our spectroscopic analysis and those reported in the literature (Table 2).

well as specific isochrones adjusted to these parameters by Bressan et al. (2012). However, there is an exception in the case of the cluster NGC 6664, where the age reported by Dias et al. (2021) significantly differs from other values found in the literature. In this particular case, we adopted the values determined by Alonso-Santiago et al. (2020) for NGC 6664, as our results will be compared with their findings in the subsequent sections. The bolometric correction values (BC_K) were determined using polynomials provided by Masana, Jordi & Ribas (2006), while an extinction ratio of $A_K/A_V = 0.112$ was adopted from Cox (2000, and references therein), and distances estimated by Dias et al. (2021) were assumed. We adopted solar values of $M_{bol} = 4.75$ mag, log $g = 4.44$ dex, and $T_{eff} = 5777$ K.

The atmospheric parameter results are displayed in Table 2, and a comparison with values reported in prior literature can be found in Fig. 2. In general, our results align well with those from previous studies (see a discussion detailed in Section 3.1). Additionally, we performed a comprehensive comparison between the spectroscopic and photometric T_{eff} and log g results obtained in our study. This critical assessment enables us to gauge the agreement between the two methods in determining the effective temperature and surface gravity, which are fundamental for understanding a star's physical properties and chemical abundances. The comparison reveals a mean absolute deviation (MAD) of 92 K and 0.09 dex for effective temperature and surface gravity, respectively, signifying a satisfactory overall agreement between the methods. Nevertheless, we acknowledge that certain discrepancies may arise due to factors such as inaccuracies in the approximation of the mean cluster reddening and distance (e.g. differential reddening and other inherent cluster-specific variations).

2.2 Chemical abundances determination

In this study, we employed two distinct methodologies to derive the abundances of the spectroscopic binary stars under investigation. These methods encompass equivalent width measurements and spectral synthesis techniques. Specifically, for the determination of abundances to five elements (C, N, O, Li, and Eu), we employed spectral synthesis analysis. The spectral synthesis approach involves a comparative analysis of the observed stellar spectrum with a model spectrum that incorporates the absorption lines for the specific element of interest. By adjusting the abundance of the element within the model spectrum until a match is achieved between the observed and model spectra, we can quantify the abundance of that particular element within the star (as illustrated in four cases depicted in Fig. 3). Conversely, for the remaining elements, we employed equivalent width measurements. The comprehensive line list, equivalent width measurements, and relevant references are available as supplementary material online.

To perform the spectral synthesis, we followed a step-by-step procedure described by Drake et al. (2002) and therein references. Specifically, we adopted the C_2 (0, 1) band head of the Swan system $A^3\Pi g - X^3\Pi u$ at 5635 Å, (as described by Lambert 1978; Huber & Herzberg 1979) to obtain ^{12}C abundances. To determine N abundances and $^{12}C/^{13}C$ isotopic ratios, we used line profiles of the CN lines of the (2, 0) band of the red system $A^2\Pi - X^2\Sigma$ in the 8002–8006 Å wavelength range (as described by Sneden & Lambert 1982). The wavelengths of the ^{12}CN lines were taken from Davis & Phillips (1963), while those of the ^{13}CN lines were taken from Wyller (1966). We also determined oxygen abundances using the [O I] line at 6300 Å, with the log gf value taken from Allende Prieto, Lambert & Asplund (2001).

We obtained the europium abundance by analysing the Eu II line at λ6645, taking into account the hyperfine splitting information from Mucciarelli et al. (2008). To determine the abundance of lanthanum, we used the MOOG drive BLENDS and equivalent widths from a complex spectral feature. Our La line list was constructed using atomic parameters from Lawler et al. (2001) and Roriz et al. (2021). To determine the Li abundance, we used the

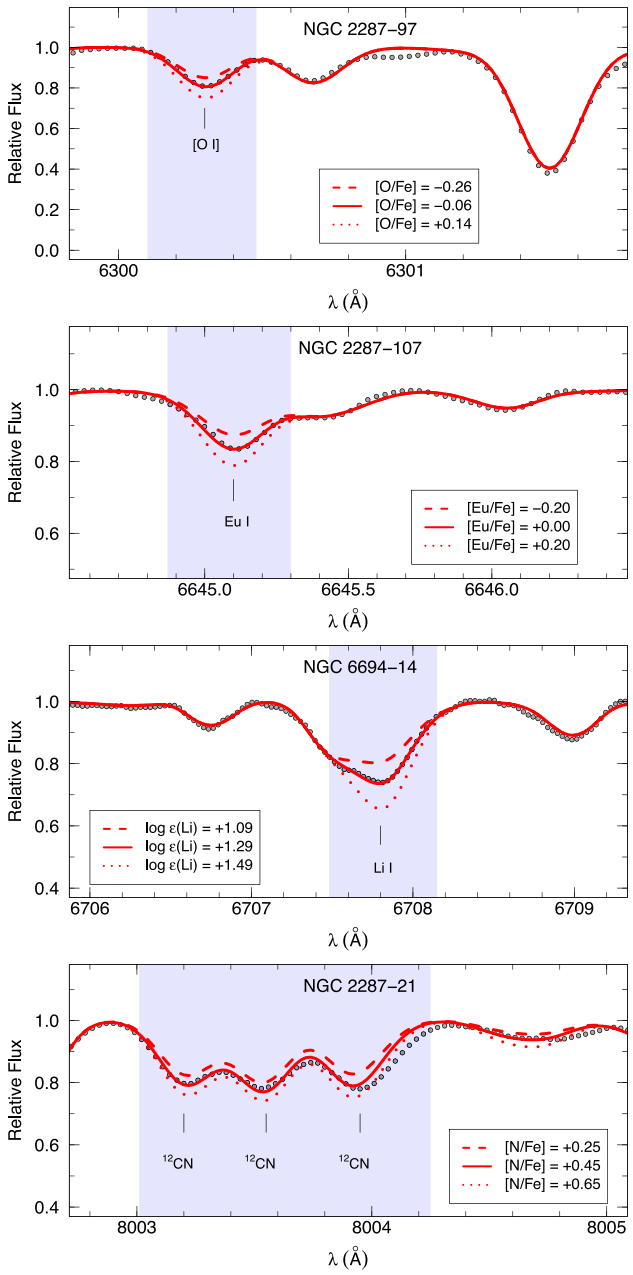

Figure 3. Best-fitting (solid lines) obtained between the synthetic and the observed FEROS spectra (circles) around Li, N (^{12}CN), O, and Eu lines regions. Two additional lines (±0.20 dex; dashed and dotted lines) are presented for comparison.

Li I λ 6708 Å, resonance doublet in our synthetic spectra, assuming LTE conditions. We also considered the presence of CN lines in the vicinity of the doublet in our line list. The hyperfine and isotopic components of the Li line were taken into account, with their respective wavelengths and oscillator strengths obtained from Smith, Lambert & Nissen (1998) and Hobbs, Thorburn & Rebull (1999).

It is important to note that non-local thermodynamic equilibrium (NLTE) effects can significantly impact the optical classical lines of Li and Na species, and should not be neglected in the abundance analysis. Therefore, we obtained 1D NLTE abundance corrections for Li using the NLTE line formation calculations available in the INSPECT data base.[1] These calculations are based on the model atom described in Lind, Asplund & Barklem (2009), which includes the most important atomic processes that affect the formation of the Li 6708 Å line in cool stars. The NLTE corrections for Li are positive for the stars analysed here, with a mean abundance correction of about + 0.30 dex. We also applied NLTE corrections for the Na lines at 4751, 6154, and 6160 Å, based on the information provided by Lind et al. (2011). These 1D NLTE corrections yielded a negative differential abundance correction for all stars in the sample. All abundance results for the light elements and the carbon isotopic ratio is compiled in Table 3, while other chemical abundances are shown in Table 4.

We assessed the impact of errors in the stellar atmospheric parameters on the uncertainties in abundance determinations. This involved varying these parameters based on their standard errors and analysing how the resulting changes affected the element abundances. This technique was applied to both the abundances obtained from equivalent widths and those derived through spectrum synthesis. Additionally, we calculated the abundance uncertainties resulting from errors in the measurements of equivalent widths using the formula given by Cayrel (1988). The errors in the equivalent widths are primarily determined by SNR and spectral resolution. In our study, the expected uncertainties in the equivalent widths are approximately 3 mÅ. The variations are presented in Table 5, where the seventh column represents the mean-squared error, and the eighth column represents the standard deviation for the chemical abundances measured with more than one line.

Table 3. Lithium and CNO abundances and carbon isotopic ratio for the target stars.

Star	log ε(Li) LTE	log ε(Li) NLTE	[C/Fe]	[N/Fe]	[O/Fe]	^{12}C/^{13}C
IC 2488-97	+0.81	+1.13	−0.27	+0.31	−0.17	32
IC 2714-34	+0.55	+0.87	+0.00	+0.25	+0.15	13
NGC 2215-26	+0.70	+0.90	−0.03	+0.34	+0.01	10
NGC 2287-21	+0.53	+0.95	−0.30	+0.45	−0.10	20
NGC 2287-97	+0.22	+0.54	−0.15	+0.40	−0.06	25
NGC 2287-107	+0.91	+1.23	+0.00	+0.35	+0.05	30
NGC 2335-4	+0.55	+0.75	+0.04	+0.28	−0.01	22
NGC 2423-43	+0.35	+0.49	−0.10	+0.30	−0.10	20
NGC 2548-1560	+0.50	+0.82	+0.01	+0.16	−0.07	30
NGC 2925-92	+0.65	+0.85	−0.20	+0.40	−0.18	23
NGC 2972-14	−0.15	+0.29	−0.25	+0.50	−0.13	23
NGC 6067-240	+0.15	+0.50	−0.10	+0.70	+0.00	20
NGC 6664-52	−0.15	+0.33	−0.40	+0.30	−0.20	25
NGC 6664-53	−0.45	−0.01	−0.20	+0.35	−0.15	26
NGC 6664-54	+0.75	+1.06	−0.07	+0.35	−0.10	20
NGC 6694-14	+1.19	+1.51	+0.03	+0.40	+0.00	25
NGC 6709-303	+1.05	+1.37	−0.09	+0.38	−0.08	25

3 DISCUSSION

3.1 Atmospheric parameters from the literature

Previous studies have analysed the atmospheric parameters of seven stars in our sample. Our analysis, which incorporates both spectroscopic and photometric methods, yielded a consistent set of atmospheric parameters for these stars. Additionally, we compiled

[1] http://www.inspect-stars.com/

Table 4. Chemical abundances of elements from Na to Eu.

[X/Fe]	IC 2488-97	IC 2714-34	NGC 2215-26	NGC 2287-21	NGC 2287-97	NGC 2287-107	NGC 2335-4	NGC 2423-43	NGC 2548-1560
Na I	+0.29	+0.26	+0.29	+0.28	+0.25	+0.26	+0.25	+0.26	+0.29
Na I_{NLTE}	+0.25	+0.15	+0.15	+0.17	+0.22	+0.24	+0.18	+0.11	+0.24
Mg I	−0.04	+0.25	+0.21	+0.19	+0.12	+0.11	+0.18	−0.17	+0.01
Al I	−0.06	+0.11	−0.07	+0.11	+0.06	−0.02	+0.02	−0.24	+0.12
Si I	+0.25	+0.34	+0.12	+0.24	+0.21	+0.16	+0.19	+0.09	+0.21
Ca I	+0.09	+0.11	+0.06	−0.11	−0.01	+0.07	+0.10	−0.07	+0.10
Ti I	−0.03	+0.08	+0.01	−0.06	−0.06	−0.11	−0.08	−0.39	−0.08
Cr I	−0.08	+0.10	+0.10	+0.07	+0.10	+0.06	+0.11	−0.23	+0.09
Ni I	+0.11	+0.08	+0.11	−0.09	+0.00	−0.04	+0.10	−0.21	+0.11
Y II	+0.09	+0.20	−0.06	+0.14	+0.12	+0.06	+0.11	+0.04	+0.21
Zr I	−0.14	+0.00	+0.25	+0.07	+0.06	−0.01	+0.15	−0.14	+0.05
La II	+0.18	+0.28	+0.12	+0.27	+0.25	+0.20	+0.27	−0.10	+0.22
Ce II	+0.18	+0.22	+0.16	+0.15	+0.15	+0.16	+0.20	+0.19	+0.17
Nd II	+0.17	+0.26	+0.15	+0.16	+0.20	+0.18	+0.25	+0.20	+0.22
Eu II	+0.00	+0.20	+0.10	+0.04	+0.14	+0.20	+0.07	−0.10	+0.08
iron-peak	+0.01	+0.09	+0.11	−0.01	+0.05	+0.01	+0.11	−0.22	+0.10
α	+0.07	+0.19	+0.10	+0.07	+0.07	+0.06	+0.10	−0.14	+0.06
s	+0.10	+0.19	+0.12	+0.16	+0.16	+0.12	+0.20	+0.04	+0.17
[X/Fe]	NGC 2925-92	NGC 2972-14	NGC 6067-240	NGC 6664-52	NGC 6664-53	NGC 6664-54	NGC 6694-14	NGC 6709-303	–
Na I	+0.27	+0.03	+0.43	+0.31	+0.30	+0.30	+0.01	+0.29	–
Na I_{NLTE}	+0.17	+0.00	+0.22	+0.28	+0.23	+0.17	−0.03	+0.27	–
Mg I	−0.05	−0.08	+0.14	−0.05	+0.14	+0.19	+0.19	+0.18	–
Al I	−0.02	−0.04	−0.02	+0.25	+0.22	+0.10	−0.03	+0.04	–
Si I	+0.09	+0.26	+0.41	+0.34	+0.00	+0.27	+0.25	+0.21	–
Ca I	+0.06	−0.12	−0.14	+0.11	+0.05	−0.02	+0.13	+0.10	–
Ti I	−0.02	−0.13	−0.08	−0.16	+0.16	+0.06	+0.08	−0.04	–
Cr I	+0.07	+0.10	−0.02	+0.09	+0.09	+0.08	−0.05	+0.10	–
Ni I	+0.05	−0.03	+0.07	+0.05	+0.02	+0.07	−0.07	+0.09	–
Y II	−0.04	−0.05	+0.04	+0.25	+0.03	+0.22	+0.20	+0.05	–
Zr I	−0.08	−0.14	−0.18	−0.18	+0.03	+0.13	+0.22	+0.17	–
La II	+0.13	−0.04	−0.05	+0.02	+0.15	+0.28	+0.29	+0.24	–
Ce II	−0.05	−0.19	+0.00	+0.06	+0.09	+0.16	+0.23	+0.14	–
Nd II	−0.03	+0.19	+0.10	+0.25	+0.07	+0.22	+0.21	+0.04	–
Eu II	−0.08	+0.09	+0.12	−0.05	+0.10	+0.19	+0.05	+0.13	–
iron-peak	+0.06	+0.04	+0.03	+0.07	+0.06	+0.08	−0.06	+0.10	–
α	+0.02	−0.02	+0.08	+0.06	+0.09	+0.13	+0.16	+0.11	–
s	−0.01	−0.05	−0.02	+0.08	+0.07	+0.20	+0.23	+0.13	–

Table 5. Typical abundance variations for the star IC 2488-97 caused by uncertainties in each atmospheric parameter.

[X/Fe]	ΔT_{eff} +80 K	$\Delta \log g$ +0.20	Δ Fe I +0.09	$\Delta \xi_t$ +0.10 km s^{-1}	ΔW_λ +3 mÅ	$(\sum\sigma^2)^{1/2}$	σ_{obs}
Li I	+0.15	+0.02	+0.03	+0.00	–	0.15	–
C (C_2)	−0.07	+0.03	+0.04	+0.05	–	0.10	–
N (CN)	+0.05	+0.10	+0.05	−0.03	–	0.13	–
O I	+0.03	+0.11	+0.03	+0.05	–	0.12	–
Na I	+0.07	+0.00	−0.01	−0.04	+0.05	0.10	0.08
Mg I	+0.03	+0.02	+0.00	−0.04	+0.05	0.07	0.05
Al I	+0.05	+0.00	−0.01	−0.03	+0.05	0.08	0.11
Si I	+0.03	+0.08	+0.03	−0.02	+0.06	0.11	0.05
Ca I	+0.09	−0.01	−0.01	−0.07	+0.05	0.13	0.11
Ti I	+0.12	−0.01	−0.01	−0.09	+0.07	0.17	0.09
Cr I	+0.08	+0.00	+0.00	−0.04	+0.05	0.10	0.15
Ni I	+0.04	+0.06	+0.03	−0.07	+0.05	0.12	0.12
Y II	+0.01	+0.11	+0.05	−0.06	+0.07	0.15	0.14
Zr I	+0.16	+0.00	−0.01	−0.04	+0.05	0.17	0.08
La II	+0.04	+0.11	+0.05	−0.02	+0.05	0.14	0.13
Ce II	+0.03	+0.11	+0.05	−0.07	+0.08	0.16	0.06
Nd II	+0.03	+0.11	+0.05	−0.03	+0.07	0.15	0.15
Eu II	+0.05	+0.11	+0.07	+0.02	–	0.14	–

literature values for chemical abundances for a sub-set of five stars. The results of our analysis, presented in Table 2, confirm the consistency of our derived atmospheric parameters with the literature values. However, we also identified some minor discrepancies, which we discuss in detail.

3.1.1 NGC 2287

Previous analysis of stars #21 and #97 in the NGC 2287 cluster was conducted by Santos et al. (2012). Our results for the atmospheric parameters show good agreement with Santos et al.'s results for T_{eff}^{spec} and [Fe/H] values while revealing significant differences for log *g* and ξ_t values. These differences could be attributed to several factors, such as the different atomic line lists and different *gf*-values for the same lines. The line lists measured by Santos et al. (2012) are significantly larger compared to our measurements for the same stars, however, their results exhibit a notable standard deviation in the mean [Fe/H] value for star #21 ($\sigma_{Fe\,I} = 0.24$ and $\sigma_{Fe\,II} = 0.37$ dex). Notably, our spectroscopic analysis yielded more accurate results for log *g* compared to the log *g* photometric findings for these two stars (in both cases Santos et al. 2012 overestimated the values of surface gravity).

3.1.2 NGC 2335

The star #4 in this cluster was previously analysed by Van der Swaelmen et al. (2017). They derived the effective temperature using the photometric calibrations of Bessell, Castelli & Plez (1998), log g value was derived from its definition $g = GM/R^2$, the metallicity was adopted from the WEBDA data base[2], and the microturbulence velocity was assumed 1.5 km s^{-1} for all stars in their sample of binary red giants. In general, our results show good agreement with their findings for the atmospheric parameters, except for a notable difference in the microturbulent velocity, which is $\Delta\xi_t = 0.75\,\mathrm{km\,s^{-1}}$.

3.1.3 NGC 2548

The star #1560 (also identified as star #8) was previously studied by Gilroy (1989) in the context of carbon isotope ratios and lithium abundance in open cluster giants. There is good concordance between our results and Gilroy's results for $T_{\rm eff}^{\rm spec}$, log g, and [Fe/H] parameters, but there is divergence in ξ_t value. This difference could be attributed to the different methodologies used in determining the microturbulent velocity. Another possible cause could be related to the different quality of the spectra used in each study, such as the SNR and spectral resolution.

3.1.4 NGC 6067

We found significant discrepancies in the log g and ξ_t values of the star #240 in the cluster NGC 6067, which was previously studied by Alonso-Santiago et al. (2017). While our effective temperature and [Fe/H] results are in relatively good agreement with theirs, the differences in the other parameters suggest that our method may be more reliable. Specifically, our log g value agrees with the evolutionary or photometric one, which provides a stronger basis for our analysis. In contrast, Alonso-Santiago et al. (2017) fixed their microturbulent velocity according to calibration from Adibekyan et al. (2012a). This difference of $\Delta\xi_t = 0.22\,\mathrm{km\,s^{-1}}$ contribute to a notable divergence in chemical abundance results, as will be discussed in Section 3.3.

3.1.5 NGC 6664

This young cluster has three stars (#52, #53, and #54) that were analysed by Alonso-Santiago et al. (2020). However, their methodology was different from ours, which led to differences in the obtained results (Table 2 and Fig. 2). The SNR was around 60 and R was approximately 85 000. Furthermore, the original line list used by Alonso-Santiago et al. (2020) comprised around 230 neutral iron lines and about 50 single ionized iron lines. Additionally, the codes of spectral analysis and atmosphere models adopted by Alonso-Santiago and colleagues were different from ours. The values of the ξ_t parameter were fixed according to an empirical relation of microturbulent velocity as a function of effective temperature and surface gravity taken from Dutra-Ferreira et al. (2016).

3.2 Projected rotational velocities

The determination of stellar rotation is crucial for understanding some aspects of stellar evolution theory and internal structure. The projected rotational velocity, v sin i, is a helpful characteristic used for inferring rotation. In this study, we estimated the influence of rotational velocity on some chemical abundances of the analysed giants by determining their v sin i using the spectral synthesis of a set of isolated absorption lines: Fe I 5778.45, Fe I 5848.12, Fe I 6027.05, Fe II 6147.70, V I 6151.50, Fe I 6187.99, and Fe I 7720.70 Å. We adopted a fixed macroturbulent velocity of 3.0 km s^{-1}, in line with the approach taken by Fekel (1997) for G and K giants. Additionally, we accounted for the instrumental broadening corresponding to the FEROS spectral resolution, which has an approximate full width at half-maximum (FWHM) of 0.13. This method has consistently yielded v sin i values that align with those from various other sources in the literature, as discussed by Holanda et al. (2021). We used an iterative procedure to determine v sin i by minimizing the deviation between the synthetic and observed spectra, as shown in Fig. 4 for the star NGC 6694-14.

To compare our v sin i measurements with those reported in previous studies, we searched for stars in common with the NGC 6664 study by Alonso-Santiago et al. (2020). We identified three stars (#52, #53, and #54) in their sample with v sin i values that are in agreement with our measurements (see Table 6). For star NGC 6067-240, Alonso-Santiago et al. (2017) only provided an upper limit of v sin i $< 5.5\,\mathrm{km\,s^{-1}}$, which is consistent with our measurement of v sin i $= 4.20 \pm 0.17\,\mathrm{km\,s^{-1}}$.

The agreement between our v sin i measurements and those from the literature strengthens the reliability of our method. Despite employing different techniques, the consistency of the results suggests that our approach provides accurate estimates of the projected rotational velocities for the analysed stars.

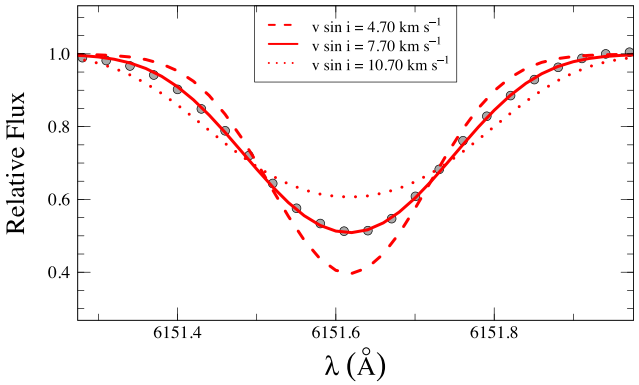

Figure 4. The projected rotational velocity (v sin i) for the star NGC 6694-14. The observed spectrum is represented by circles and the best-fitting is shown in a solid line.

Table 6. Projected rotational velocities (in km s^{-1}) for sample stars in comparison with results from the literature.

	NGC 6664		
	#52	#53	#54
This work	6.47 ± 0.15	4.10 ± 0.17	5.27 ± 0.21
Alonso-Santiago et al. (2020)	6.10 ± 0.80	4.30 ± 0.50	5.50 ± 1.00

[2]WEBDA is a site devoted to open star clusters and is the Web version of the database known as BDA. Available on https://webda.physics.muni.cz/

3.3 Chemical abundances

3.3.1 Metallicity

The understanding of stellar metallicity in open clusters plays a crucial role in investigating the chemical behaviour of the Galaxy and stellar evolution. While the metallicity in the Galactic disc generally decreases with increasing distance from the Galactic centre, deviations from this trend have been observed in certain cases, highlighting the complexity of Galactic chemical evolution (e.g. Netopil et al. 2016). In this study, we determined the metallicity [Fe/H] for all spectroscopic binary stars by measuring their equivalent widths and normalizing them based on the solar abundance derived by Asplund et al. (2009), where $\log \varepsilon(\mathrm{Fe})_{\odot} = +7.50$ dex. Additionally, we compared our [Fe/H] results with the mean metallicity of each of the 13 open clusters under investigation. This allowed us to examine potential systematic differences between our measurements and previous studies, as well as variations in the metallicity among stars within each cluster. Our results exhibit a high level of concordance with the mean metallicity values reported in the existing literature for the studied open clusters, assuming homogeneity among the constituent stars within each cluster. This concordance is further discussed below.

The open cluster IC 2714 has received limited attention in terms of chemical analysis in the literature, with most sources focusing primarily on metallicity. The first study of this cluster was conducted by Claria et al. (1994), providing a mean metallicity of [Fe/H] $= -0.12 \pm 0.09$ dex. Two more recent articles by Heiter et al. (2014) and Tsantaki et al. (2023) found mean values of [Fe/H] $= +0.02 \pm 0.06$ dex (four stars) and [Fe/H] $= -0.06 \pm 0.02$ dex (eight stars), respectively. In this context, our result for star #34 moderately agrees with Claria et al. (1994), who analysed 204 stars in IC 2714 based on *UBV* photoelectric photometry.

For the open cluster IC 2488, Clariá et al. (2003) observed 119 stars in the field, including 3 red giant stars, and obtained a mean [Fe/H] value of $+0.10 \pm 0.06$ dex. Our result for the star IC 2488-97, [Fe/H] $= +0.15 \pm 0.09$, is in good agreement with this finding. However, for the less studied open cluster NGC 2215, Fitzgerald et al. (2015) determined a metallicity of [Fe/H] $= -0.40 \pm 0.10$ dex using a methodology based on photometric data. This result significantly deviates from our finding for star #26, where we obtained a metallicity of [Fe/H] $= -0.04$ dex using high-resolution spectroscopic analysis. It is worth noting that differences in the adopted methodologies, such as photometric-based metallicity determination versus spectroscopic analysis, may contribute to the observed discrepancies in the metallicity measurements for NGC 2215.

The metallicity of NGC 2287 was analysed by Santos et al. (2009), Heiter et al. (2014), and Tsantaki et al. (2023), who obtained mean values of -0.17 ± 0.08 dex (two stars), -0.11 ± 0.01 dex (two stars), and -0.14 ± 0.02 dex (four stars), respectively. These results are consistent with our findings for three stars, yielding a mean metallicity of -0.10 ± 0.08 dex. Our results are also aligned with the low-metallicity dispersion found in the Galactic globular clusters and in the magellanic clouds clusters (e.g. Lardo et al. 2022; Narloch et al. 2022). Additionally, Mermilliod, Mayor & Udry (2008) present a very low dispersion of the mean radial velocities for these three SB1 stars in this cluster. Regarding NGC 2423, Heiter et al. (2014) and Tsantaki et al. (2023) reported the values of $+0.08 \pm 0.05$ dex (two stars) and -0.03 ± 0.06 dex (four stars), respectively. On the other hand, our study found a solar metallicity for binary #43, indicating agreement with both references.

The giant star #11 in NGC 2335 was analysed by Reddy, Giridhar & Lambert (2013), who reported a metallicity of [Fe/H] $= -0.19 \pm 0.04$ dex. However, Twarog, Ashman & Anthony-Twarog (1997) obtained a different result of [Fe/H] $= -0.03 \pm 0.09$ dex based on photometric data. Our findings for star #4 lie between these two references and are in agreement with both. For NGC 2548 (also known as Messier 48), Sun et al. (2020) found a mean metallicity of [Fe/H] $= -0.06 \pm 0.01$ dex, which is consistent with our result for star #1560 (-0.07 ± 0.10). However, significant differences arise in the case of NGC 2925, where our analysis shows a metallicity difference for star #92 of $+0.31 \pm 0.13$ dex compared to the mean value of [Fe/H] $= -0.01 \pm 0.01$ dex reported by Tsantaki et al. (2023). Similarly, for NGC 2972, our result for star NGC 2972-14 of [Fe/H] $= -0.17$ dex does not agree with the mean value of [Fe/H] $= +0.04$ dex (two stars) obtained by Tsantaki et al. (2023).

In the case of NGC 6067, Tsantaki et al. (2023) found a high dispersion in the metallicities of the three stars analysed, with a mean value of $+0.20 \pm 0.26$ dex. Although such a high dispersion is not common in open clusters, our result for star #240 agrees with this high metallicity value.

As previously mentioned by Alonso-Santiago et al. (2020), the cluster NGC 6664 presents metallicity of -0.04 ± 0.10 dex. Our analysis, which includes three stars, shows excellent agreement with the mean derived by them, resulting in [Fe/H] $= -0.04 \pm 0.14$ dex. Even though the derived [Fe/H] dispersion is relatively larger than the one found by Alonso-Santiago et al. (2020), it is still within the expected metallicity dispersion found in stellar clusters; first-generation stars in globular clusters can show metallicity variations between 0.05 and 0.30 dex (Lardo et al. 2022), while magellanic clouds star clusters show metallicity dispersions between 0.10 and 0.30 (Narloch et al. 2022). We analysed three stars classified by Mermilliod, Mayor & Udry (2008) as members of the cluster. These stars require long-term observations (RV values agree within the uncertainties from the mean) and it is well known that binarity can affect astrometric analysis. For instance, star #54 exhibits a parallax value of 0.6391 mas (Gaia Collaboration 2023), while the cluster has an average parallax of 0.473 mas (Dias et al. 2021). However, *Gaia* DR3 provides a renormalized unit weight error (RUWE) value of 1.614 for this star. A RUWE value >1.4 could indicate that the source is significantly affected by binarity or other issues affecting the astrometric solution, potentially resulting in unreliable astrometric results. In this sense, the classification made by Mermilliod, Mayor & Udry (2008) appears to be the most reliable result in the context of membership analysis. Moreover, the individual metallicities of these three stars are compatible within the uncertainties.

Finally, the open cluster NGC 6709 has received little attention in the literature, and our study of star #303 represents the most comprehensive chemical analysis to date. Unfortunately, there are no existing articles on the chemical composition of this cluster to compare with our results.

3.3.2 Lithium

In red giants, the first dredge-up occurs when the convective envelope penetrates the partially processed inner layers, resulting in a fresh supply of material reaching the surface. This leads to altered photospheric abundances of some elements, including a decrease in ^{12}C abundance and an increase in ^{14}N and ^{13}C abundances. Additionally, the first dredge-up causes Li depletion by a factor of approximately 2 orders of magnitude, due to the dilution by Li-depleted material

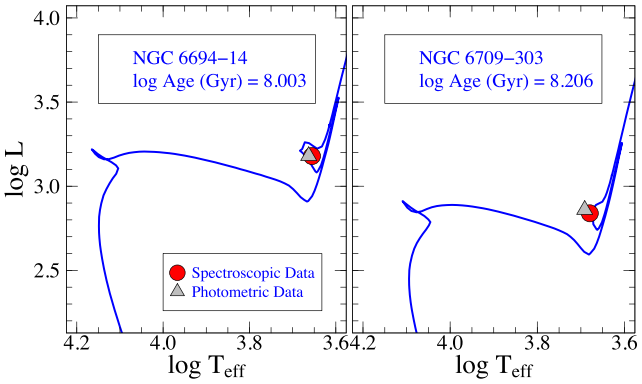

Figure 5. The H–R diagrams of the open clusters with the star most enhanced in lithium. The isochrones are taken from the PARSEC tracks (Bressan et al. 2012) and ages obtained from Dias et al. (2021). The circles represent the position of stars when we adopt spectroscopic parameters and the triangles photometric parameters.

previously processed in the interior. This decrease in Li abundance is a useful indicator of the depth of the convective envelope and is commonly used to constrain stellar evolution models (e.g. Karakas & Lattanzio 2014).

The majority of giant stars have very low Li abundances, typically several orders of magnitude lower than in the interstellar medium from which they originated. However, there are rare cases of Li-rich giants that may have undergone an extra-mixing process, merger with He dwarf companion, brown dwarf or planetary accretion, or binary interactions (e.g. de la Reza et al. 1997; Siess & Livio 1999a; Aguilera-Gómez et al. 2016; Zhou et al. 2018 2021; Casey et al. 2019; Zhang et al. 2020; Holanda, Drake & Pereira 2020a, b). The classical low limit for Li-rich giants is log ε(Li) $\geq$ 1.5 dex, and the origin and survival of Li in the atmosphere of these stars is still debated. Identifying Li-rich stars in open clusters can be useful, since clusters provide constraints on the mass and age of their members, offering a unique opportunity to understand the evolutionary stage where the enrichment occurs and make it possible to trace the evolution of Li in the Galactic disc. This, in turn, allows to determine a specific Li abundance limit for giant stars based on the abundance of their progenitors (Delgado Mena et al. 2016; Randich et al. 2020; Magrini et al. 2021; Romano et al. 2021; Tsantaki et al. 2023).

Within our sample of stars, one star stands out due to its surprisingly high abundance of lithium, although it only just crosses the classical limit to be considered Li-rich. Star NGC 6694-14 presents an unusual abundance of log ε(Li) = 1.51 dex, coupled with an anomalous v sin i value of 7.5 km s^{-1}. Similarly, star NGC 6709-303 also exhibits this intriguing combination of characteristics, although its enrichment in Li is somewhat less pronounced (1.37 dex), and its v sin i value is 7.1 km s^{-1}. In fact, among the giant stars we analysed, those with log ε(Li) > 1.30 dex represent only 4 per cent of the sample reported by Brown et al. (1989). Although the correlation between Li enrichment and high rotation remains a topic of debate (see Drake et al. 2002; Du et al. 2021; Magrini et al. 2021), it is possible that an episode of planetary engulfment or accretion of a companion could result in a substantial increase in v sin i and Li abundance, as suggested by Siess & Livio (1999b). Under this scenario, the planet or brown dwarf companion may be swallowed during the red giant branch (RGB) or the asymptotic giant branch (AGB) stage.

Fig. 5 displays positions of stars NGC 6694-14 and NGC 6709-303 on the Hertzsprung–Russell diagram based on their spectroscopic and photometric parameters ($T_{\rm eff}$ and log g). The ages of these clusters were determined by Dias et al. (2021), and the turn-off masses for the respective isochrones (PARSEC; Bressan et al. 2012) were used to calculate their luminosities. These stars are likely in the post-RGB ascension phase but have not yet reached the early-AGB stage, making it unlikely that accretion or engulfment events have occurred in the context of explaining some Li-enrichment. Furthermore, since these stars were not objects with degenerate He-cores, speculations about extra-mixing triggered by He flash can also be dismissed – the clusters NGC 6694 and NGC 6709 have turn-off masses of 5.09 and 4.22 M$_{\odot}$, respectively.

One plausible explanation for the observed enrichment of lithium in these stars is the tidal interaction, as discussed by Casey et al. (2019). In essence, they propose that the internal production of lithium is triggered by a tidal spin-up caused by a binary companion. The authors have also identified that most of the Li-rich giants in their sample possess He-burning cores. Our findings on anomalous rotational velocities, as detailed in Section 3.5, provide additional support for this hypothesis.

Moreover, our results for the Li abundance show excellent agreement with the findings of Alonso-Santiago et al. (2020; refer to Table 7 of this paper). It is worth noting that despite the considerable number of studies investigating the abundance of lithium in stars within open clusters, there remains a substantial gap in the literature concerning the determination and comparison of results about this particular element.

3.3.3 *Carbon, nitrogen, and oxygen*

The process of dredge-up in RGB stars, involving the transportation of products from H-burning to the stellar surface, exerts a profound influence on the abundances of nitrogen, carbon, and the ^{12}C/^{13}C isotopic ratio within their atmospheres. These indicators of mixing provide valuable insights into the extent of envelope mixing triggered by stellar evolution and serve as effective tools for studying these processes (Takeda et al. 2019). While the abundance of carbon and nitrogen can undergo significant alterations due to internal processes and mixing events, the abundance of oxygen remains relatively stable.

The CNO abundances derived from our analysis of the sample of spectroscopic binaries provide compelling evidence that these objects have experienced the first dredge-up, a phenomenon consistent with the abundances observed in single/normal giant stars. Notably, we determined relatively 'low' values for the carbon isotopic ratio in stars IC 2714-34 and NGC 2215-26, as shown in Table 3. These clusters, IC 2714 and NGC 2215, are among the oldest clusters in our sample, with turn-off mass values of 2.8 and 2.3 M$_{\odot}$, respectively (Bressan et al. 2012; Dias et al. 2021). It is generally expected to observe low ^{12}C/^{13}C values in stars within this mass range, and our results align reasonably well with the thermohaline and rotation model proposed by Lagarde et al. (2012). The agreement between our findings and the theoretical predictions reinforces our understanding of the dredge-up process, the occurrence of extra mixing, and the specific mass range in which these phenomena take effect.

3.3.4 *Sodium and aluminum*

In our study, we investigated the abundance of the odd-Z elements sodium and aluminum. Regarding Na, we found a notable enrichment in our sample of giant stars, as depicted in Fig. 6. This enrichment is consistent with previous observational studies, such as the work by

Table 7. The chemical abundances obtained in this study and in the literature. Abundances taken from the literature were re-normalized to the solar abundances by Asplund et al. (2009). Note that the abundances are presented as ratios relative to iron, except for lithium which is traditionally expressed as log ε(Li). References: AS17, Alonso-Santiago et al. (2017), AS20, Alonso-Santiago et al. (2020), G89, Gilroy (1989), and VS17, Van der Swaelmen et al. (2017).

[X/Fe]	NGC 2335-4	NGC 6067-240	NGC 6664-52	NGC 6664-53	NGC 6664-54	Ref.
O I	+0.04	−0.17	−0.25	−0.15	−0.10	This work
	–	−0.14	–	–	–	AS17
	–	–	−0.20 ± 0.12	−0.23 ± 0.04	+0.27 ± 0.11	AS20
Na I	+0.18	+0.22	+0.28	+0.23	+0.30	This work
	–	−0.19	–	–	–	AS17
	–	–	−0.17 ± 0.42	−0.10 ± 0.44	−0.24 ± 0.14	AS20
Mg I	+0.18	+0.14	−0.05	+0.14	+0.19	This work
	–	–	−0.18 ± 0.06	+0.28 ± 0.01	−0.21 ± 0.06	AS20
Si I	+0.19	+0.41	+0.35	+0.00	+0.27	This work
	–	+0.28	–	–	–	AS17
	–	–	0.52 ± 0.09	+0.57 ± 0.08	+0.17 ± 0.19	AS20
Ca I	+0.10	−0.14	+0.18	+0.05	−0.02	This work
	–	−0.38	–	–	–	AS17
	–	–	−0.01 ± 0.19	−0.07 ± 0.09	+0.32 ± 0.09	AS20
Ti I	−0.0–8	−0.08	−0.16	+0.16	+0.06	This work
	–	−0.36	–	–	–	AS17
	–	–	−0.17 ± 0.28	+0.02 ± 0.10	+0.22 ± 0.16	AS20
Ni I	+0.10	+0.07	+0.05	+0.02	+0.07	This work
	–	−0.07	–	–	–	AS17
	–	–	+0.10 ± 0.09	+0.07 ± 0.10	+0.15 ± 0.13	AS20
Y II	+0.11	−0.05	+0.25	+0.03	+0.22	This work
	+0.46 ± 0.53	–	–	–	–	VS17
	–	–	+0.14 ± 0.51	+0.04 ± 0.17	+0.41 ± 0.08	AS20
La II	+0.04	−0.05	+0.02	+0.15	+0.28	This work
	+0.20 ± 0.08	–	–	–	–	VS17
Ce II	+0.20	+0.00	+0.06	+0.09	+0.16	This work
	+0.27 ± 0.22	–	–	–	–	VS17
Nd II	+0.25	+0.10	+0.25	+0.07	+0.22	This work
	+0.66	–	–	–	–	VS17
Li I*	+0.75	+0.50	+0.33	−0.01	+1.06	This work
	–	+0.06 ± 0.18	–	–	–	AS17
	–	–	–	–	+1.03 ± 0.09	AS20

Holanda et al. (2022), which confirm an increase in Na abundance in intermediate-mass giant stars (>2.0 $M_\odot$) that has been widely discussed in the literature. Theoretical investigations, such as the study by Lagarde et al. (2012), also support the notion of enhanced Na abundance in giants of intermediate to higher masses. Specifically, we selected the thin disc stars analysed by Adibekyan et al. (2012b) for comparison, they used high-resolution spectra to provide abundance results for a wide range of chemical elements, including Na, Mg, Al, Si, Ca, Ti, Cr, and Ni. Concerning Al abundances, our analysis revealed agreement between the Al abundance values in our sample and those derived from a large sample studied by Adibekyan et al. (2012b). The observed agreement indicates the consistency of aluminum abundance measurements across various metallicities within our sample.

It is worth noting that Alonso-Santiago et al. (2020) examined three stars in the open cluster NGC 6664 and determined the sodium abundance for these stars using a different methodology (Table 7). Additionally, the values of $T_{\rm eff}$ and the fixed $\xi_{\rm t}$ value adopted from Alonso-Santiago et al. (2017) may contribute to the substantial difference observed in the Na abundances of the star NGC 6067-240, as they constitute the primary sources of uncertainty. For an illustration of how these parameters impact Na abundance, see Table 5. These notable discrepancies between their results and ours underscore the importance of further investigation into the factors influencing Na abundance variations across different methodologies.

3.3.5 *α- and iron-peak elements*

α-Elements and iron-peak elements are two groups of elements that play an essential role in the study of stellar nucleosynthesis and galactic chemical evolution. α-Elements, including O, Mg, Si, and Ca, are produced in massive stars during explosive nucleosynthesis events, such as supernovae. The production of α-elements occurs on a short time-scale, typically on the order of a few million years. On the other hand, iron-peak elements, such as Fe, Ni, and Cr, are primarily produced through explosive nucleosynthesis during the final stages of an intermediate-mass star's life, such as during Type Ia supernovae (Kobayashi, Karakas & Lugaro 2020). The production of iron-peak elements is associated with a longer time-scale compared to the α-elements, typically on the order of hundreds of millions of years.

In Fig. 6, we compare the abundances obtained for our sample of SB stars with the abundances found by Adibekyan et al. (2012b) for dwarf stars of the thin disc. While there is good overall concordance between the two samples of stars in terms of distribution or trend for α- and iron-peak element abundances, except for the [Si/Fe] and [Ti/Fe] distributions. It is important to consider that differences in methodology could contribute to some variations in the abundance ratios. Two key factors that can lead to differences in abundance measurements are the choice of line list and *gf*-values used for spectral analysis.

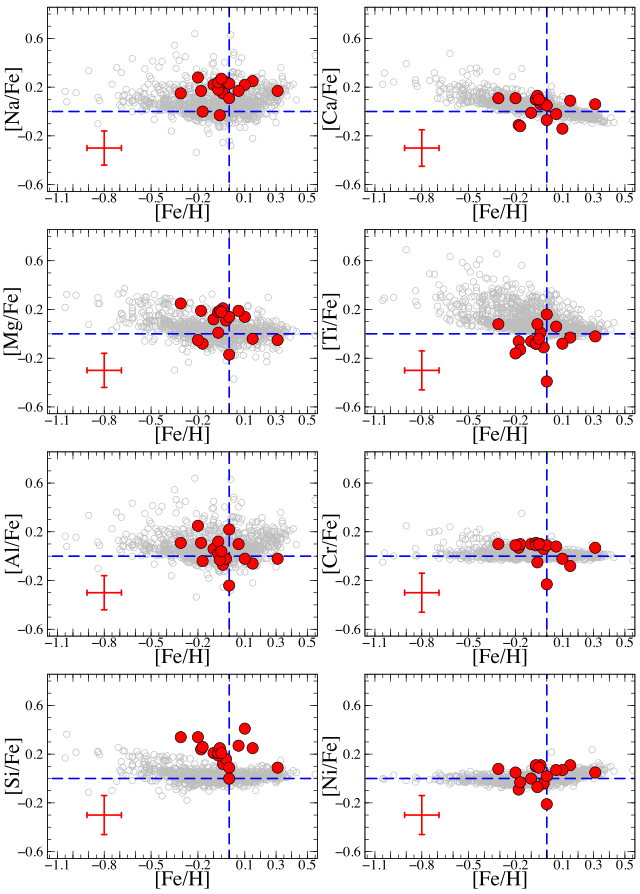

Figure 6. Abundance ratios [X/Fe] versus [Fe/H]. The filled circles represent our sample, the open circles represent the sample of dwarf stars from the thin disc (Adibekyan et al. 2012b), and the dashed lines indicate the solar value.

Additionally, a similar difference is found by Alonso-Santiago et al. (2020) when they compare [Si/Fe] ratios derived for five young open clusters, including NGC 6067 and NGC 6664, with the sample studied by Adibekyan et al. (2012b). However, our result for the [Ca/Fe] ratio is aligned with the trend observed by Adibekyan et al. (2012b), while Alonso-Santiago et al. (2020) identify a similar difference for [Si/Fe] and [Ca/Fe] ratios. Concerning [Ti/Fe], our results tend to be located at the bottom of the distribution of stars analysed by Adibekyan et al. (2012b). The same occurs for the results obtained by Alonso-Santiago et al. (2020) for the clusters NGC 6649 and NGC 6664. However, when considering uncertainties in this distribution, a match between the two samples is observed.

3.3.6 Heavy elements

The formation of heavy elements encompasses a diverse range of astrophysical environments where intricate processes occur. Among these, neutron capture plays a pivotal role by facilitating the absorption of neutrons into atomic nuclei, leading to the synthesis of heavier isotopes. Neutron capture can be categorized into two primary modes: the slow process (*s*-process) and the rapid process (*r*-process). The *s*-process unfolds gradually over long time-scales, involving sequential neutron captures and beta decays, predominantly resulting in the generation of relatively lighter heavy elements. In contrast, the *r*-process occurs rapidly within highly neutron-rich environments, where intense neutron fluxes trigger rapid neutron

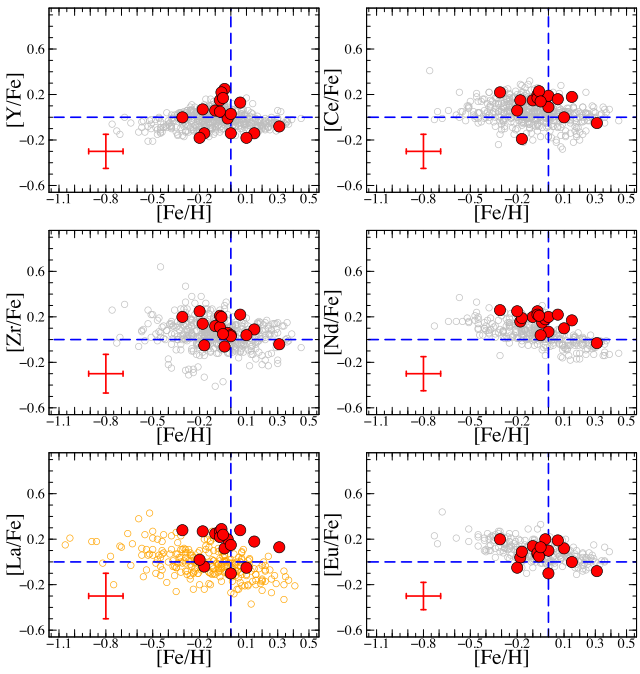

Figure 7. Abundance ratios for *s*- and *r*-process elements [X/Fe] versus [Fe/H]. The grey and orange circles represent the samples analysed by Battistini & Bensby (2016) and Delgado Mena et al. (2017), respectively.

captures and subsequent beta decays, enabling the production of elements higher up the periodic table (Burbidge et al. 1957; Busso, Gallino & Wasserburg 1999; Thielemann et al. 2011). In our study, we employed two methods to determine the abundance of specific heavy elements. The equivalent width technique was used to accurately measure the abundances of Y II, Zr I, La II, Ce II, and Nd II. Furthermore, we employed spectral synthesis to derive the abundance of Eu II.

Delgado Mena et al. (2017) conducted an extensive study of FGK dwarf stars using high-resolution spectra ($R \approx 115\,000$) and provided chemical abundances for Cu, Zn, Sr, Y, Zr, Ba, Ce, Nd, and Eu. These results serve as a valuable reference for our comparative analysis of thin disk trends. Additionally, we incorporate the data set analysed by Battistini & Bensby (2016) in our comparison, focusing on La abundances. In their work, Battistini & Bensby (2016) performed an analysis using high-resolution spectra obtained from the MIKE and FEROS spectrographs. Fig. 7 presents the comparison between our findings and the results from Delgado Mena et al. (2017) and Battistini & Bensby (2016). We specifically concentrate on the abundances of Zr, Y, La, Ce, Nd, and Eu. Our analysis reveals a slight enrichment in our sample for the elements La, Ce, and Nd, while the abundance of Eu exhibits excellent agreement. However, when comparing the abundances of Y and Zr, we observe a significant dispersion for the stars in our sample. Given the associated uncertainties, no definitive trend can be identified that either aligns with or contradicts the results of Delgado Mena et al. (2017).

It is widely documented in the literature that there exists a correlation between the abundance of *s*-process elements and the age of stars. First, D'Orazi et al. (2009) observed a pronounced increasing trend in barium abundance (a prominent representative of *s*-process elements) as a function of cluster age. Subsequently, Maiorca et al. (2011, 2012) confirmed these findings and expanded the analysis to include other *s*-process elements such as Y, Zr, La, and Ce. Despite

this well-established trend, there is still no definitive explanation. However, one possible clue lies in the enhanced production of neutron-capture nuclei by low mass AGB stars (see D'Orazi et al. 2022). Nevertheless, several studies have observed enrichment in *s*-process elements for stars belonging to young open clusters (single or not), which also seems to occur for the SB stars of open clusters analysed in this work.

3.4 Yellow straggler candidates

YSs are stars that exhibit unusually bright and yellow colours compared to other stars in their cluster. They are stars with a mass greater than that of regular subgiants in the same cluster and are believed to form from binary star interactions, where two stars in a binary system can transfer mass between them (Anthony-Twarog, Twarog & Sheeran 1994; Landsman et al. 1997; Portegies Zwart et al. 1997). Additionally, Mermilliod et al. (2007a) suggests that the presence of a companion can also affect the position of a red giant star in CMD, as the combined colours of a red giant with a bluer main-sequence companion may place the system within the subgiant branch. More recently, Rani et al. (2023) confirms the binary nature of YS stars through a spectral energy distribution study. They found that hot components are likely to be A-type sub-dwarfs, which confirms the spectral appointments in some previous works, as da Silveira, Pereira & Drake (2018) and Martinez et al. (2020), which identify contamination in spectra of giant stars, therefore indicating a hot dwarf star as likely companion in YS systems. Ebbighausen (1939), Skiff (1987, 2014), and Harris et al. (1993) previously indicated the possibility of a composite spectra configuration in the stars NGC 2287-102 and NGC 2548-1260. In Fig. 8, we present the spectral region between 3750 and 4000 Å, for these selected stars, contrasting them with individual G- and A-type spectrum stars.[3] This comparison is focused exclusively on the spectral shape, as there were no investigations of atmospheric parameters.

In a recent study, Rain, Ahumada & Carraro (2021) meticulously compiled a valuable catalogue through an extensive membership assessment, encompassing 897 BSs and 77 YS candidate stars that were observed within 111 open clusters. Within this catalogue, YSs were identified in 43 clusters and subjected to proper motion decontamination to ensure the unambiguous identification of YS candidates. It is important to note that Rain, Ahumada & Carraro (2021) characterizes YSs as objects that display a significant upward displacement of the isochrone by 0.75 mag, as this criterion aids in identifying the loci of equal-mass binaries. Furthermore, the authors established an age threshold of log Age $\sim$ 8.7 for the occurrence of BS stars in open clusters, which corresponds to the absence of stragglers in very young clusters. In this context, Fig. 9 illustrates the positions of the two YSs identified in our study on CMDs, with due consideration given to the estimated age, extinction, and distance of the cluster, as provided by Dias et al. (2021).

3.4.1 NGC 2287-102

In their comprehensive analysis, Kervella et al. (2019) extensively utilized the HIPPARCOS and *Gaia* catalogues (van Leeuwen 2007; Gaia Collaboration 2018) to scrutinize the presence of proper motion anomalies stemming from stellar or sub-stellar companions around a nearby star. The NGC 2287-102 system yielded

[3]Spectra of the stars HD 65810 and HD 85552 were sourced from the ESO Library Spectra: https://www.eso.org/public/

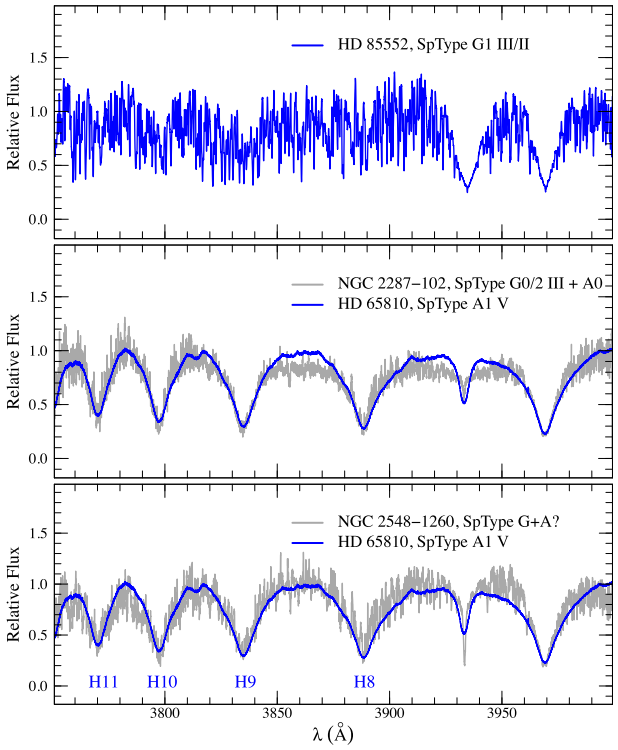

Figure 8. A spectra comparison. In grey, the yellow straggler candidates of our sample, NGC 2287-102 and NGC 2548-1260. In blue, the normalized spectra of a G-type template star (upper; HD 85552) and a hot dwarf star (HD 65810) for comparison. Information about spectral types was taken from the literature (Ebbighausen 1939; Harris et al. 1993; Skiff 2014).

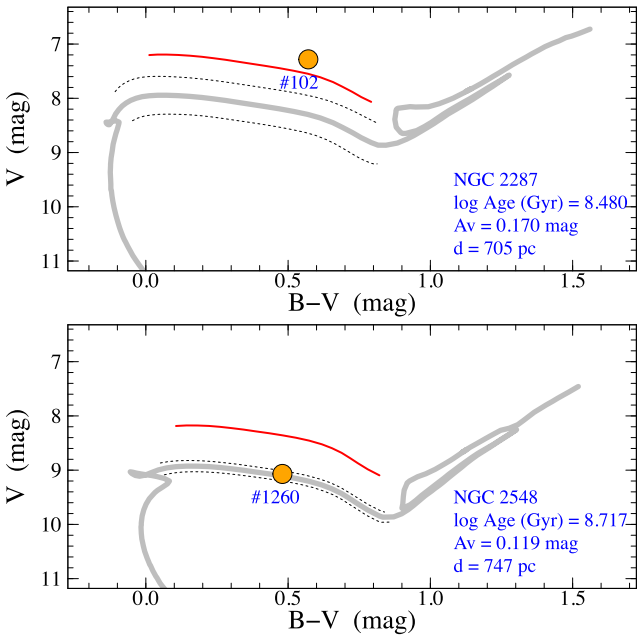

Figure 9. The CMD displays the YS candidates identified in two open clusters, NGC 2287 and NGC 2548. The cluster parameters were extracted from Dias et al. (2021), and for the analysis, we employed the corresponding isochrones from Bressan et al. (2012). The best-fitting isochrones are illustrated as thick solid lines, while the uncertainties are represented by dotted lines. Additionally, the thin solid (red) line indicates a displacement of 0.75 mag from the best-fitting isochrone, a commonly adopted criterion for encompasses binary systems with stars of equal mass.

intriguing results, with the primary star estimated to have a mass of $M_A = 5.172 \pm 0.259\,M_\odot$ and the companion estimated at $M_B = 159.54^{+53.68}_{-34.44}\,M_{JUP}$. Notably, the mass of the primary star was found to be overestimated in relation to the cluster's turn-off mass, which stands at $M_{\text{turn-off}} \sim 3.2\,M_\odot$ when the age of the cluster is log Age (Gyr) = 8.48. Moreover, in their membership analysis based on *Gaia* data, Cantat-Gaudin et al. (2020) flagged this star as a probable member, with an astrometric probability of 0.9.

Upon careful examination of the NGC 2287-102 spectrum, distinct signatures of its companion become evident, as illustrated in Fig. 8. This is particularly noticeable in the shape of H-absorption lines when compared to a hot dwarf star, as the contribution of a hot companion primarily affects the bluer and ultraviolet regions of the composite spectra, a finding consistent with the observations reported by Rani et al. (2023) and others. Previously, Harris et al. (1993) conducted an examination of star #102 and identified indications of a composite or variable spectrum in their data.

Furthermore, its position in the CMD plot (Fig. 9) lies above the limit of 0.75 mag, a limit adopted for identifying close binary systems composed of stars with equal mass (represented by the red line). This 'high' luminosity aligns with the concept of YSs, as presented by Rain, Ahumada & Carraro (2021) in their catalogue. However, it is essential to acknowledge that uncertainties in the isochrone fitting process may contribute to the interpretation of any deviations observed along the isochrone line, considering that YSs are expected to exhibit greater brightness.

3.4.2 NGC 2548-1260

In a recent study by Zhang et al. (2021), which focused on stellar populations within open clusters, the peculiar star labelled as #1260 was investigated. The authors determined its atmospheric parameters as follows: $T_{\text{eff}} = 5200$ K, log $g = 3.18$ dex, [Fe/H] $= -0.07$ dex, and $\xi = 0.4\,\text{km s}^{-1}$. Notably, the microturbulent velocity value for this star is exceptionally low, indicating contamination in its spectrum, which can be associated with the YS phenomenon (a similar finding is reported by Sales Silva et al. 2014). Among the 40 red giant/clump stars investigated across 18 open clusters by Zhang et al. (2021), this star exhibits the lowest microturbulent velocity value. Fig. 8 shows the spectrum of this star, highlighting it as one of the contaminated YS spectra.

The position of star #1260 on the CMD (Fig. 9) indicates it lies within the Hertzsprung's gap, yet its brightness matches the isochrone from Dias et al. (2021). We have also considered uncertainties in the isochrone fitting process, represented by the dotted lines, but even when accounting for these uncertainties, star #1260 does not exhibit a significantly 'high' brightness compared to the normal stars indicated by the isochrone. An early study by Ebbighausen (1939) classified this star as F 2p, implying a probable composite G+A spectrum according to Trumpler's classification. Our findings corroborate this ancient study, as we have identified a set of H-lines with a shape similar to that of a hot dwarf star, similar to what was observed in NGC 2287-102's spectrum.

3.5 Orbital parameters

The study of orbital parameters, including the orbital period (P) and eccentricity (e), is crucial for understanding the effects of mass transfer on the formation, evolution, and unique properties of binary systems. Mass transfer episodes can lead to intriguing phenomena such as changes in the chemical composition and evolutionary paths

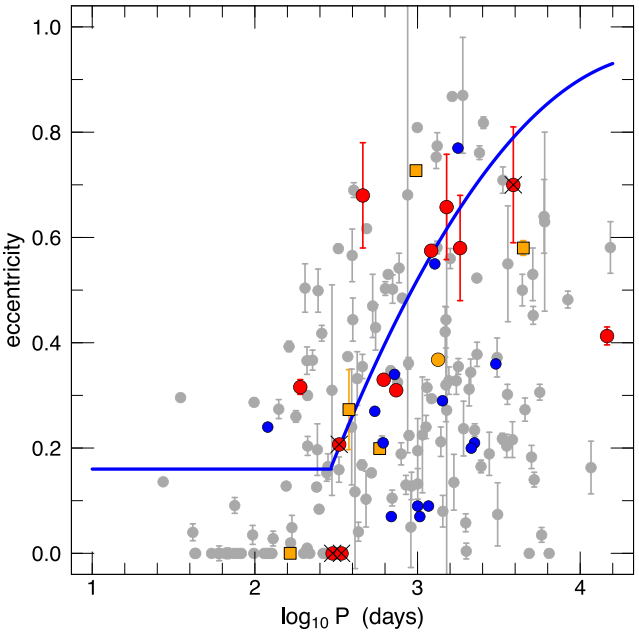

Figure 10. log P – eccentricity diagram for red giant stars in open clusters (Mermilliod et al. 2007a). The stars studied in this work are identified as big yellow circles (YSs) and big red circles, and '×' indicates the stars with $v \sin i \geq 6\,\text{km s}^{-1}$. The squares represent YSs identified by Sales Silva et al. (2014), da Silveira, Pereira & Drake (2018), and Martinez et al. (2020), while small (blue) circles represent single-lined BSs studied by Gosnell et al. (2015). The inner (blue) line region is characteristic of mass-transfer binary systems, as Ba stars analysed in Van der Swaelmen et al. (2017).

of the involved stars. This understanding is particularly significant when investigating the formation of chemically peculiar objects like Li-rich giants and Ba stars, which can result from tidal interactions (as discussed in Section 3.3.2) and mass-transfer processes, respectively.

In a previous study, Van der Swaelmen et al. (2017) investigated the mass function distribution among binary red giants in open clusters and compared it with that of Ba stars. The study unveiled a consistent pattern, where barium stars, on average, showcased lower eccentricity values for a given orbital period. A more specific examination zoomed in on a sub-set of binary giant stars in open clusters, sharing a location on the log P–e diagram similar to that of the barium stars, and displaying companion masses typical of white dwarfs. Within this constrained sample, approximately 33 per cent of the binary red giants in open clusters displayed a chemical signature indicating mass transfer, as evidenced by a moderate and strong overabundance of s-process elements. In Fig. 10, the blue line demarcates the concentration of barium stars (as defined by Van der Swaelmen et al. 2017) that exhibit enrichment of s-process elements.

Fig. 10 presents the SB1 systems with orbital solutions as determined by Mermilliod et al. (2007a). The analysed (sub)sample is indicated by red and yellow circles on the plot. We have also included yellow squares to represent the YSs identified in previous works by Sales Silva et al. (2014), da Silveira, Pereira & Drake (2018), and Martinez et al. (2020). Notably, these YSs were previously examined by Mermilliod et al. (2007a) in their survey. Moreover, we have incorporated single-lined BSs studied by Gosnell et al. (2015) in the context of the open cluster NGC 188. The YSs and BSs are concentrated within the region demarcated by the blue line. This region is a characteristic feature of S and Ba stars, which are objects

Table 8. Orbital periods and eccentricities obtained by Mermilliod et al. (2007b). Additionally, v sin i values obtained in this work via spectral analysis are shown.

Star	P d	e	v sin i km s^{-1}
NGC 2215-26	190.207	0.316	3.1
NGC 2287-21	1509.600	0.658	3.3
NGC 2287-97	461.070	0.680	3.8
NGC 2287-102	1337.600	0.368	–
NGC 2287-107	1212.600	0.575	4.0
NGC 2335-4	300.760	0.000*	7.3
NGC 2423-43	1827.000	0.580	3.8
NGC 2548-1560	14624.000	0.413	3.4
NGC 2925-92	619.270	0.330	3.0
NGC 2972-14	340.860	0.000*	6.9
NGC 6664-54	739.290	0.310	5.3
NGC 6694-14	3880.000	0.700	7.5
NGC 6709-303	329.849	0.207	7.1

*Note.**Fixed value.

that have undergone enrichment via mass transfer from an evolved companion. In their study, Van der Swaelmen et al. (2017) categorize objects as Ba stars when their [X/Fe] ratios exceed +0.25 dex, with X representing elements like Y, La, Ce, or Nd. Additionally, the author proposes that an 'outlier' Ba star could be identified as a mild Ba star if it exhibits at least two abundance ratios surpassing this threshold.

In our study, we have identified seven stars that occupy the same region on the log P–e diagram as the barium stars. Specifically, in the case of IC 2714-34, it displays [La/Fe] and [Nd/Fe] ratios of +0.28 and +0.26, respectively, which would categorize it as a mild barium star according to the criteria set by Van der Swaelmen et al. (2017). However, the lack of an available orbital solution restricts us from conducting a more comprehensive analysis in this context. Additionally, de Castro et al. (2016) proposed that a star should possess a mean [s/Fe] ratio equal to or higher than +0.25 dex to be classified as a Ba star. In this context, IC 2714-34 would not be categorized as a barium star due to its [s/Fe] ratio of +0.19. Among the stars examined in our study, NGC 6694-14 exhibits the highest mean [s/Fe] ratio, at +0.23. However, even though it presents a relatively elevated [s/Fe] ratio, it falls short of the criteria required to be labelled as a Ba star.

In our analysis of the YSs' spectra, we did not find evidence of enrichment in *s*-process species, supporting the scenario of an unevolved companion, as discussed in Section 3.4. However, it is important to note that we were unable to determine atmospheric parameters due to the high contamination present in these spectra, which systematically affects the Fe I/Fe II lines, with more significant impact observed in the bluer part of the spectrum, as also noted by Sales Silva et al. (2014) for the YSs they analysed.

We observed four stars with anomalous v sin i values (indicated by '×' in Fig. 10) and occupying the region indicative of mass-transfer systems. Mass transfer in binaries can lead to high values of v sin i due to the transfer of angular momentum – compared to single stars, non-interacting binaries, or non-mass-transfer binaries. Additionally, it is noteworthy that the stars NGC 6694-14 and NGC 6709-303 exhibit both anomalous v sin i values and Li enrichment, indicating that binary interaction is the most likely scenario to explain this unusual features. Low eccentricities and orbital periods corroborate this scenario (see these parameters in Table 8).

4 SUMMARY

Our extensive analysis employing high-resolution FEROS spectra of the 17 single-lined spectroscopic binary giants and two yellow straggler stars in 15 open galactic clusters can be summarized as follows:

(i) We conducted a comprehensive analysis of atmospheric parameters, projected rotational velocities, and chemical abundances for a sample of 17 single-lined spectroscopic binaries. Our investigation encompassed 20 chemical species, allowing for a thorough characterization of their properties. Additionally, our study revealed the presence of two yellow straggler stars exhibiting contaminated spectra, which do not allow for determining atmospheric parameters and chemical abundances.

(ii) We observed a similar trend in our sample of spectroscopic binaries compared to the analysis conducted by Adibekyan et al. (2012b) on dwarf stars from the thin disc. However, small differences were noted in the abundances of Na, Si, and Ti. Specifically, the Na abundances in intermediate-mass stars in the post-main-sequence stage were found to be higher compared to dwarfs. This can be attributed to Na acting as a reliable mixing tracer, as supported by numerous observational and theoretical findings in the literature. About Si over iron, the trend observed in the results of Adibekyan et al. appears to be flatter when compared to our sample of binary stars. However, it is important to consider that this discrepancy may be influenced by the uncertainties associated with our results, particularly due to the prominent inclination observed in the distribution of abundances in the [Fe/H] versus [Si/Fe] plot.

(iii) Additionally, we took into account the results obtained by Delgado Mena et al. (2017) and Battistini & Bensby (2016), who analysed the photospheric composition of heavy elements (Zr, La, Ce, Nd, and Eu) in dwarf stars from the solar neighbourhood. Our analysis revealed a slight enrichment in *s*-process elements, such as La, Ce, and Nd, which further supports the hypothesis of *s*-process enrichment in red giant stars belonging to young open clusters. In this case, we extended the investigation to one-lined spectroscopic binaries. Furthermore, when examining the abundance of 'pure' *r*-process element Eu, we found excellent agreement between the spectroscopic binary giant stars and the dwarf stars analysed by Delgado Mena et al. (2017).

(iv) Our research has yielded significant findings regarding the presence of Li enrichment in giant stars. Specifically, we have identified two giants, including NGC 6694-14, with Li abundances surpassing the traditional limit for low-mass Li-rich giants (+1.50 dex). To gain a deeper understanding of this phenomenon, we conducted a comprehensive analysis that took into account multiple factors, such as the stars' positions in the colour–magnitude diagram, projected rotational velocities, and orbital periods and eccentricities analysis. The most likely cause of the observed Li enrichment in these two stars is tidal interaction, which aligns with the scenario proposed by Casey et al. (2019) as the most common formation mechanism for Li-rich giants. Supporting evidence includes anomalous rotational velocities, circular orbits, and relatively 'short' orbital periods.

(v) We reaffirm that YSs are peculiar objects that are formed as a consequence of binarity in a stellar cluster context. Occasionally, these stars are commonly regarded as potential later stages of BSs, which are more well-known in the literature. Their investigation and study play a crucial role in comprehending their formation and evolution in stellar cluster scenarios. However, in a composite of YS systems, only (sub)dwarf companions have been identified (e.g. da Silveira, Pereira & Drake 2018; Martinez et al. 2020; Rani et al. 2023), contrasting with BSs where binarity remains unconfirmed in

some instances. In our current research, we identified clear signs of contamination in the spectra of the giant component in the YS candidate systems NGC 2287-102 and NGC 2548-1260. These stars lie within Hertzsprung's gap of their respective CMDs and display pronounced hot star signatures in the bluer regions of their spectra, consistent with the hypothesis of a composite system comprising a giant G/K-type star and a dwarf A-type star. Specifically, NGC 2287-102 exhibits higher brightness compared to the normal evolutionary path indicated by the cluster's isochrone. Although this characteristic aligns with the typical traits of YSs, it is notably sensitive to uncertainties associated with the isochrone fitting process.

(vi) Despite being derived from a limited number of stars, we observed an intra-cluster metallicity scatter of approximately 0.1 dex in both NGC 2287 and NGC 6664. This scatter remains consistent whether we consider our derived values or those from the literature for the stars' metallicities. Additionally, intra-cluster abundances exhibit a similar scatter, possibly reaching up to 0.15 dex. Further investigation is required to determine whether these variations can be attributed to chemical inhomogeneities within the progenitor cloud or are a consequence of the cluster's evolutionary processes.

ACKNOWLEDGEMENTS

We would like to thank the referee for constructive comments and suggestions which helped in improving the manuscript. This study was financed in part by the Coordenação de Aperfeiçoamento de Pessoal de Nível Superior – Brasil (CAPES) – Finance Code 001. NH acknowledges fellowships 300181/2023-0 and 304315/2023-0 of the PCI Program – Ministério da Ciência, Tecnologia e Inovação (MCTI) and Conselho Nacional de Desenvolvimento Científico e Tecnológico (CNPq). NAD acknowledges Fundação de Amparo á Pesquisa do Estado do Rio de Janeiro – FAPERJ, Rio de Janeiro, Brazil, for grant E-26/203.847/2022. FFSM acknowledges financial support from CNPq (404482/2021-0) and FAPERJ (E-26/211.475/2021 and E-26/201.386/2022). SD acknowledges CNPq for grant PQ 306859/2022-0.

This study is also based on the observations made with the 2.2 m telescope at the European Southern Observatory (La Silla, Chile) under the agreement between Observatório Nacional and Max-Planck Institute für Astronomie.

DATA AVAILABILITY

Data are available on request. The data underlying this article will be shared on reasonable request to the corresponding author.

REFERENCES

Adibekyan V. Z., Delgado Mena E., Sousa S. G., Santos N. C., Israelian G., González Hernández J. I., Mayor M., Hakobyan A. A., 2012a, A&A, 547, A36
Adibekyan V. Z., Delgado Mena E., Sousa S. G., Santos N. C., Israelian G., González Hernández J. I., Mayor M., Hakobyan A. A., 2012b, A&A, 547, A36
Aguilera-Gómez C., Chanamé J., Pinsonneault M. H., Carlberg J. K., 2016, ApJ, 829, 127
Albrow M. D., Ulusele I. H., 2022, MNRAS, 515, 730
Allende Prieto C., Lambert D. L., Asplund M., 2001, ApJ, 556, L63
Alonso A., Arribas S., Martínez-Roger C., 1999, A&AS, 140, 261
Alonso-Santiago J., Negueruela I., Marco A., Tabernero H. M., González-Fernández C., Castro N., 2017, MNRAS, 469, 1330
Alonso-Santiago J., Negueruela I., Marco A., Tabernero H. M., Castro N., 2020, A&A, 644, A136
Anthony-Twarog B. J., Twarog B. A., Sheeran M., 1994, PASP, 106, 486
Asplund M., Grevesse N., Sauval A. J., Scott P., 2009, ARA&A, 47, 481
Battistini C., Bensby T., 2016, A&A, 586, A49
Bessell M. S., Castelli F., Plez B., 1998, A&A, 333, 231
Boffin H. M., Carraro G., Beccari G. et al., 2015, Ecology of Blue Straggler Stars. 0067-0057Vol. 413, Springer Berlin, Heidelberg,
Bond H. E., 2019, ApJ, 887, 12
Bressan A., Marigo P., Girardi L., Salasnich B., Dal Cero C., Rubele S., Nanni A., 2012, MNRAS, 427, 127
Brown J. A., Sneden C., Lambert D. L., Dutchover Edward J., 1989, ApJS, 71, 293
Burbidge E. M., Burbidge G. R., Fowler W. A., Hoyle F., 1957, Rev. Mod. Phys., 29, 547
Busso M., Gallino R., Wasserburg G. J., 1999, ARA&A, 37, 239
Cantat-Gaudin T. et al., 2020, A&A, 640, A1
Casey A. R. et al., 2019, ApJ, 880, 125
Castelli F., Kurucz R. L., 2004, Proc. IAU Symp. 210, Modelling of Stellar Atmospheres, Astron. Soc. Pac., San Francisco, p. A20
Cayrel R., 1988, in Cayrel de Strobel G., Spite M.eds, Vol. 132, The Impact of Very High S/N Spectroscopy on Stellar Physics, Kluwer Academic Publishers, Dordrecht, p. 345
Claria J. J., Mermilliod J. C., Piatti A. E., Minniti D., 1994, A&AS, 107, 39
Clariá J. J., Piatti A. E., Lapasset E., Mermilliod J. C., 2003, A&A, 399, 543
Cox A. N., 2000, Allen's Astrophysical Quantities, Springer Science and Business Media, New York
de Castro D. B., Pereira C. B., Roig F., Jilinski E., Drake N. A., Chavero C., Sales Silva J. V., 2016, MNRAS, 459, 4299
de la Reza R., Drake N. A., da Silva L., Torres C. A. O., Martin E. L., 1997, ApJ, 482, L77
da Silveira M. D., Pereira C. B., Drake N. A., 2018, MNRAS, 476, 4907
D'Orazi V., Magrini L., Randich S., Galli D., Busso M., Sestito P., 2009, ApJ, 693, L31
D'Orazi V., Baratella M., Lugaro M., Magrini L., Pignatari M., 2022, Universe, 8, 110
Davis S. P., Phillips J. G., 1963, The Red System (A2[pi]-X2[Sigma]) of the CN Molecule. Univ. California Press, Berkeley
Delgado Mena E. et al., 2016, A&A, 587, A66
Delgado Mena E., Tsantaki M., Adibekyan V. Z., Sousa S. G., Santos N. C., González Hernández J. I., Israelian G., 2017, A&A, 606, A94
Dias W. S., Monteiro H., Moitinho A., Lépine J. R. D., Carraro G., Paunzen E., Alessi B., Villela L., 2021, MNRAS, 504, 356
Drake N. A., de la Reza R., da Silva L., Lambert D. L., 2002, AJ, 123, 2703
Du M.-h., Bi S.-l., Shi J.-r., Yan H.-l., 2021, Chinese Astron. Astrophys., 45, 45
Duchêne G., Kraus A., 2013, ARA&A, 51, 269
Dutra-Ferreira L., Pasquini L., Smiljanic R., Porto de Mello G. F., Steffen M., 2016, A&A, 585, A75
Ebbighausen E. G., 1939, ApJ, 90, 689
Fekel F. C., 1997, PASP, 109, 514
Fitzgerald M. T. et al., 2015, AJ, 149, 190
Friel E. D., 1995, ARA&A, 33, 381
Gaia Collaboration, 2018, A&A, 616, A1
Gaia Collaboration, 2023, A&A, 674, A1
Gilroy K. K., 1989, ApJ, 347, 835
Gosnell N. M., Mathieu R. D., Geller A. M., Sills A., Leigh N., Knigge C., 2015, ApJ, 814, 163
Harris G. L. H., Fitzgerald M. P. V., Mehta S., Reed B. C., 1993, AJ, 106, 1533
Heiter U., Soubiran C., Netopil M., Paunzen E., 2014, A&A, 561, A93
Hekker S., Meléndez J., 2007, A&A, 475, 1003
Hobbs L. M., Thorburn J. A., Rebull L. M., 1999, ApJ, 523, 797
Holanda N., Pereira C. B., Drake N. A., 2019, MNRAS, 482, 5275
Holanda N., Drake N. A., Pereira C. B., 2020a, MNRAS
Holanda N., Drake N. A., Pereira C. B., 2020b, AJ, 159, 9
Holanda N., Drake N. A., Corradi W. J. B., Ferreira F. A., Maia F., Magrini L., da Silva J. R. P., Pereira C. B., 2021, MNRAS, 508, 5786

Holanda N., Ramos A. A., Peña Suárez V. J., Martinez C. F., Pereira C. B., 2022, MNRAS, 516, 4484
Holanda N., Drake N. A., Pereira C. B., 2023, MNRAS, 518, 4038
Huber K., Herzberg G., 1979, Molecular Spectra and Molecular Structure. Van Nostrand Reinhold Company, New York, USA
Jadhav V. V., Roy K., Joshi N., Subramaniam A., 2021, AJ, 162, 264
Jorissen A., Van Winckel H., Siess L., Escorza A., Pourbaix D., Van Eck S., 2020, A&A, 639, A7
Karakas A. I., Lattanzio J. C., 2014, PASA, 31, e030
Karinkuzhi D. et al., 2018, A&A, 618, A32
Kaufer A., Stahl O., Tubbesing S., Nørregaard P., Avila G., Francois P., Pasquini L., Pizzella A., 1999, The Messenger, 95, 8
Kervella P., Arenou F., Mignard F., Thévenin F., 2019, A&A, 623, A72
Kobayashi C., Karakas A. I., Lugaro M., 2020, ApJ, 900, 179
Lada C. J., Lada E. A., 2003, ARA&A, 41, 57
Lagarde N., Decressin T., Charbonnel C., Eggenberger P., Ekström S., Palacios A., 2012, A&A, 543, A108
Lambert D. L., 1978, MNRAS, 182, 249
Lambert D. L., Heath J. E., Lemke M., Drake J., 1996, ApJS, 103, 183
Landsman W., Aparicio J., Bergeron P., Di Stefano R., Stecher T. P., 1997, ApJ, 481, L93
Lardo C., Salaris M., Cassisi S., Bastian N., 2022, A&A, 662, A117
Lawler J. E., Wickliffe M. E., den Hartog E. A., Sneden C., 2001, ApJ, 563, 1075
Lind K., Asplund M., Barklem P. S., 2009, A&A, 503, 541
Lind K., Asplund M., Barklem P. S., Belyaev A. K., 2011, A&A, 528, A103
Magrini L., Sestito P., Randich S., Galli D., 2009, A&A, 494, 95
Magrini L. et al., 2021, A&A, 651, A84
Maiorca E., Randich S., Busso M., Magrini L., Palmerini S., 2011, ApJ, 736, 120
Maiorca E., Magrini L., Busso M., Randich S., Palmerini S., Trippella O., 2012, ApJ, 747, 53
Martinez C. F., Holanda N., Pereira C. B., Drake N. A., 2020, MNRAS, 494, 1470
Masana E., Jordi C., Ribas I., 2006, A&A, 450, 735
Mermilliod J. C., Mayor M., 1989, A&A, 219, 125
Mermilliod J. C., Andersen J., Latham D. W., Mayor M., 2007a, A&A, 473, 829
Mermilliod J. C., Andersen J., Latham D. W., Mayor M., 2007b, A&A, 473, 829
Mermilliod J. C., Mayor M., Udry S., 2008, A&A, 485, 303
Mucciarelli A., Caffau E., Freytag B., Ludwig H. G., Bonifacio P., 2008, A&A, 484, 841
Narloch W. et al., 2022, A&A, 666, A80
Netopil M., Paunzen E., Heiter U., Soubiran C., 2016, A&A, 585, A150
Peña Suárez V. J., Sales Silva J. V., Katime Santrich O. J., Drake N. A., Pereira C. B., 2018, ApJ, 854, 184
Pereira C. B., Sales Silva J. V., Chavero C., Roig F., Jilinski E., 2011, A&A, 533, A51
Portegies Zwart S. F., Hut P., McMillan S. L. W., Verbunt F., 1997, A&A, 328, 143
Rain M. J., Carraro G., Ahumada J. A., Villanova S., Boffin H., Monaco L., Beccari G., 2020, AJ, 159, 59
Rain M. J., Ahumada J. A., Carraro G., 2021, A&A, 650, A67
Randich S. et al., 2020, A&A, 640, L1
Rani S., Pandey G., Subramaniam A., Rao N. K., 2023, ApJ, 945, 11
Reddy A. B. S., Lambert D. L., 2019, MNRAS, 485, 3623
Reddy A. B. S., Giridhar S., Lambert D. L., 2013, MNRAS, 431, 3338
Romano D. et al., 2021, A&A, 653, A72
Roriz M. P., Lugaro M., Pereira C. B., Sneden C., Junqueira S., Karakas A. I., Drake N. A., 2021, MNRAS, 507, 1956
Sales Silva J. V., Peña Suárez V. J., Katime Santrich O. J., Pereira C. B., Drake N. A., Roig F., 2014, AJ, 148, 83
Santos N. C., Lovis C., Pace G., Melendez J., Naef D., 2009, A&A, 493, 309
Santos N., Lovis C., Melendez J., Montalto M., Naef D., Pace G., 2012, A&A, 538, A151
Santrich O. J. K., Pereira C. B., Drake N. A., 2013, A&A, 554, A2
Siess L., Livio M., 1999a, MNRAS, 304, 925
Siess L., Livio M., 1999b, MNRAS, 308, 1133
Skiff B. A., 1987, Inf. Bull. Var. Stars, 3009, 1
Skiff B. A., 2014, VizieR Online Data Catalog, p. B/mk
Smith V. V., Lambert D. L., Nissen P. E., 1998, ApJ, 506, 405
Sneden C. A., 1973, PhD thesis, Univ. Texas, Austin
Sneden C., Lambert D. L., 1982, ApJ, 259, 381
Sollima A., Carballo-Bello J. A., Beccari G., Ferraro F. R., Pecci F. F., Lanzoni B., 2010, MNRAS, 401, 577
Stryker L. L., 1993, PASP, 105, 1081
Sun Q., Deliyannis C. P., Steinhauer A., Twarog B. A., Anthony-Twarog B. J., 2020, AJ, 159, 220
Takeda Y., Omiya M., Harakawa H., Sato B., 2019, PASJ, 71, 119
Thielemann F. K. et al., 2011, Prog. Part. Nucl. Phys., 66, 346
Tody D., 1986, in Crawford D. L.ed., Society of Photo-Optical Instrumentation Engineers (SPIE) Conference Series Vol. 627, Instrumentation in Astronomy VI, Bellingham, WA, p. 733
Tsantaki M., Delgado-Mena E., Bossini D., Sousa S. G., Pancino E., Martins J. H. C., 2023, A&A, 674, 157
Twarog B. A., Ashman K. M., Anthony-Twarog B. J., 1997, AJ, 114, 2556
Van der Swaelmen M., Boffin H. M. J., Jorissen A., Van Eck S., 2017, A&A, 597, A68
van Leeuwen F., 2007, A&A, 474, 653
Wyller A. A., 1966, ApJ, 143, 828
Zhang X., Jeffery C. S., Li Y., Bi S., 2020, ApJ, 889, 33
Zhang R. et al., 2021, A&A, 654, A77
Zhou Y. T., Shi J. R., Yan H. L., Gao Q., Zhang J. B., Zhao G., Pan K., Kumar Y. B., 2018, A&A, 615, A74
Zhou Z.-M. et al., 2021, Res. Astron. Astrophys., 21, 020

This paper has been typeset from a TEX/LATEX file prepared by the author.